THE JOURNAL OF PHYSICAL CHEMISTRY C
A JOURNAL OF THE AMERICAN CHEMICAL SOCIETY

pubs.acs.org/JPCC

Article

Acoustic Wave Generation in Nanofluids: Effect of the Kapitza Resistance on the Thermophone to Mechanophone Generation Mechanism Transition

Stefano Giordano,* Michele Diego,* and Francesco Banfi*

Cite This: J. Phys. Chem. C 2023, 127, 10227−10244

Read Online

ACCESS | Metrics & More | Article Recommendations

ABSTRACT: High frequency, short wavelength acoustic wave generation in fluids, by means of immersed nanotransducers, is key to applications ranging from the biomedical to the ICT sector, all the way to investigating fundamental aspects of the mechanics of fluids. In this context, the commonly adopted generation mechanism is the thermophone, where the nanotransducer serves as a nanoheater for the surrounding fluid and the acoustic wave is launched by water thermal expansion. Its performance, however, is severely degraded when reaching up to hypersonic frequencies. We analytically investigate the thermoacoustic response in the frequency domain for the case of a gold nanofilm transducer in contact with water. We prove that another generation mechanism, the mechanophone, sets in this critical frequency range, widening the acoustic generation bandwidth. In the mechanophone, it is the nanotransducer thermal expansion that launches pressure waves in water. We find a threshold frequency discriminating between these two regimes, which can be tuned by acting on the Kapitza resistance at the solid−liquid interface. We then show how the mechanophone mechanism can be activated in the frame of photoacoustic generation with pulsed laser sources. The unveiled physics bears generality beyond the specific system and explains the acoustic generation mechanisms in nanofluids.

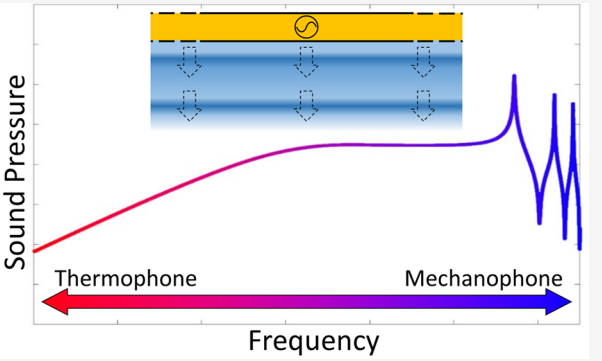

INTRODUCTION

Acoustic wave generation in fluids (both liquids and gases) is a fundamental process for both sound production systems and noninvasive imaging techniques. Its applications span across a myriad of fields, ranging from diagnostic/therapy in the biomedical sector and non-nondestructive testing in disparate industrial settings to submarine signal transmission.[1]

Since its discovery in 1880,[2] the piezoelectric effect played a key role among the several acoustic generation mechanisms.[3−8] Despite the important biomedical and engineering applications of piezoelectric materials, alternative solutions are being investigated to increase the frequency bandwidth (in water, it is limited, for both resonant and non resonant use, to about 50−200 MHz,[9,10] with some exceptions at 300 MHz[11]). For instance, a recent method is based on capacitive micromachined ultrasonic transducers (CMUTs),[12] where the acoustic wave is generated by the attraction force between the plates of a condenser, resulting in improved integrability with silicon technology, and wider bandwidth with respect to piezoelectric devices. The bandwidth limitation became a major issue with the advent of nanoresonators, which sizes, in the few tens of nanometers range, unlocked the gate to acoustic frequencies in the hypersonic frequency range.[13,14]

The search for ultra-wide-band acoustic sources, sought for dealing with meso- and nano-scale applications, led to a renewed interest in the thermophone mechanism. In its simpler form, the idea is to periodically deliver heat to a sample, i.e. the transducer, in contact with a fluid. The heat transfer from the transducer to the fluid results in a periodic temperature variation in the latter, which, through its thermal expansion, generates pressure waves in the fluid itself. This approach is fully wideband since it does not rely on any resonance phenomenon. Heat may be delivered to the transducer material in a variety of ways, the most commonly adopted being driving an electrical current through it or shining light on it. Although the generation mechanism remains the thermophone, this process is often addressed as the thermophone effect, when heat is fed electrically, and the photophone (or photothermal or photoacoustic) effect, when heat is fed via a light source. Interestingly, the latter two were discovered at the same time as the piezoelectric effect and each

Received: March 17, 2023
Revised: April 26, 2023
Published: May 23, 2023

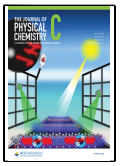

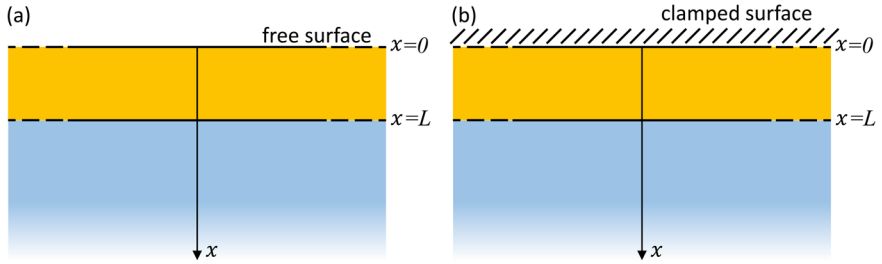

Figure 1. Au nanotrasducer on water system. The 20 nm thick Au film (yellow, $x \in [0, L]$) is in contact with a semi-infinite water layer (azure, $x \in [L, +\infty)$). The origin of the coordinate axis, $x = 0$, is at the Au film's top surface. The Au film/water interface rests at $x = L = 20$ nm. (a) Free top film surface. (b) Clamped top film surface.

one developed independently as an autonomous research field, see for instance refs 15−19 and refs 20−27 for milestones results in the history of the thermophone and photophone effects, respectively.

However, until recently, thermoacoustic generation was inefficient because of the lack of materials with good thermomechanical properties. Only lately, with the advent of nanotechnology, innovative materials were made available with high thermal conductivity and low heat capacity,[28−31] paving the way to efficient thermophone-based transducers. Without any pretension of being exhaustive, we mention efficient thermophones based on carbon nanotubes,[32−38] aluminum wires,[39] gold wires,[40] silver wires,[41] graphene,[42−46] and boron nitride foams.[47,48] Today, due to the advent of nanotechnology, the thermophone, also in its photoacoustic realization, is an object of renewed interest, mainly for its potential in imaging and therapeutic applications.[49−53] In this context, a particular effort is dedicated to the study of metal nanotransducers, which have proven to be efficient photoacoustic generators,[54] exploiting their high and tunable optical absorption properties,[55−57] high contrast imaging features,[58] and biocompatibility.[59,60]

Early quantitative photo-thermoacoustic models were developed for the efficient development of photoacoustic spectroscopy, photoacoustic microscopy, and photoacoustic imaging,[61−64] and are the basis of successive developments. In particular, in ref 64, the concept of the piston model was introduced. In this context, a great deal of effort has been devoted to modeling and improving the thermophone response in the high-frequency range.[65−77] The bottom line is that the penetration length of the thermal wave in the fluid decreases as $\omega^{-1/2}$, ω being the angular frequency with which heat power density is delivered to the nanotransducer. Thus, the capacity to generate an acoustic wave decreases accordingly, and the efficiency of the thermophone mechanism is severely degraded in the high-frequency regime.

However, propitiously, it was recently suggested that, in this high-frequency regime, a second generation mechanism intervenes, addressed as *mechanophone*.[78,79] In the thermophone, the heat transferred from the solid to the fluid generates compression and expansion processes in the fluid itself, thus launching acoustic waves in the latter. Differently, in the mechanophone, it is the heat retained in the solid that causes internal oscillations of stress and strain that are transmitted to the fluid by pure mechanical transduction, ultimately launching acoustic waves in the fluid. These aspects were numerically investigated in the time domain,[78,79] yet lack an exhaustive physical comprehension and a formulation in analytical terms. The latter is a major impediment towards uncovering the parameters combination ruling the transition from the thermophone to the mechanophone regime. This drawback ultimately prevents engineering, beyond a trial-and-error approach, efficient thermoacoustic nanotransducers operating in the high-frequency range.

We here solve the issue, by analyzing the case of a nanometric film transducer heated via a *time-harmonic* source (we adopted a 20 nm thick gold film in numerical examples). The bottom side of the film is in contact with water, the top side is either free or clamped, see Figure 1. We adopt this simple 1D geometry to investigate the thermophone vs mechanophone competition in the frequency domain. This approach allows us to formally retrieve the interplay of the parameters ruling the thermoacoustic generation in a clear, explicit form. As a matter of fact, operating with a 1D geometry in the frequency domain yields analytical solutions in relatively simple terms (e.g., exponential rather than Bessel functions, as in the case of a cylindrical system[77]). We provide evidence that there is a specific threshold frequency beyond which the mechanophone becomes more effective than the thermophone. This threshold frequency is strongly dependent on the Kapitza resistance at the nanotransducer-fluid interface, which can be controlled via interface engineering.[80] We then switch to analyzing the case of a realistic pulsed-excitation scenario. We show that the analytical results, obtained in the frame of the frequency-domain formulation, remain good predictive tools also for the photoacoustic problem triggered by a pulsed laser source. We investigate the acoustic response of the system for different values of the laser pulse duration in order to fully explore the frequency spectrum obtained in the previous analysis. We then uncover the interplay between pulse duration and Kapitza resistance and its effects on thermoacoustic generation.

THEORY

We introduce here the thermoacoustic model. We assume a solid layer (the nanotransducer), extending in the region $x \in [0, L]$ and a fluid medium (e.g., water) for $x \in [L, +\infty)$, see Figure 1. The balance equations for the fluid in one-dimensional geometry read[75,81]

$$\frac{1}{B_0}\frac{\partial p}{\partial t} = \alpha_0\frac{\partial T}{\partial t} - \frac{\partial v}{\partial x},$$

$$\rho_0\frac{\partial v}{\partial t} = -\frac{\partial p}{\partial x} + (\lambda_0 + 2\mu_0)\frac{\partial^2 v}{\partial x^2},$$

$$\rho_0 C_{p0}\frac{\partial T}{\partial t} = \kappa_0\frac{\partial^2 T}{\partial x^2} + \alpha_0 T_0\frac{\partial p}{\partial t}, \quad (1)$$

where the pressure p (Pa), the temperature T (K), and the particle velocity v (m/s) are the variables depending on time t

https://doi.org/10.1021/acs.jpcc.3c01808
J. Phys. Chem. C 2023, 127, 10227−10244

(s) and space x (m). Moreover, ρ_0 is the density (kg/m^3), B_0 the bulk modulus (Pa), α_0 the coefficient of volumetric expansion (1/K), λ_0 and μ_0 the first and second viscosity coefficients (Pa·s), C_{p0} the specific heat at constant pressure (J/(kg·K)), T_0 the ambient temperature (K), and κ_0 the thermal conductivity (W/(m·K)). All these parameters will be considered as constants in the fluid. The balance equations given in eq 1 represent the conservation laws of mass, momentum, and energy once combined with the linearized constitutive equations of the material. The linearization is justified in the present context since thermoacoustic waves are usually represented by small variations of the relevant quantities around the given equilibrium values.

For the solid layer, the balance equations are cast in the same form[75,82]

$$\frac{1}{B_1}\frac{\partial p}{\partial t} = \alpha_1\frac{\partial T}{\partial t} - \frac{\partial v}{\partial x},$$
$$\rho_1\frac{\partial v}{\partial t} = -\frac{\partial p}{\partial x} + (\lambda_1 + 2\mu_1)\frac{\partial^2 v}{\partial x^2},$$
$$\rho_1 C_{p1}\frac{\partial T}{\partial t} = \kappa_1\frac{\partial^2 T}{\partial x^2} + \alpha_1 T_0\frac{\partial p}{\partial t} + q, \quad (2)$$

where the following quantities intervene

$$B_1 = \frac{B_s}{1 - \frac{4}{3}\frac{v_T^2}{v_L^2}}, \quad (3)$$

$$\alpha_1 = \alpha_s\left(1 - \frac{4}{3}\frac{v_T^2}{v_L^2}\right), \quad (4)$$

$$C_{p1} = C_{ps}\left(1 - \frac{4}{3}\frac{v_T^2}{v_L^2}\frac{C_{ps} - C_{vs}}{C_{ps}}\right), \quad (5)$$

$$\rho_1 = \rho_s, \quad (6)$$

$$\kappa_1 = \kappa_s, \quad (7)$$

and

$$v_T = \sqrt{\frac{\mu_s}{\rho_s}}, \quad (8)$$

$$v_L = \sqrt{\frac{\lambda_s + 2\mu_s}{\rho_s}}, \quad (9)$$

$$B_s = \lambda_s + \frac{2}{3}\mu_s. \quad (10)$$

For the solid, ρ_s is the density (kg/m^3), B_s the bulk modulus (Pa), α_s the coefficient of volumetric expansion (1/K), λ_1 and μ_1 the first and second viscosity coefficients (Pa·s), λ_s and μ_s the elastic Lamé constants (Pa), C_{ps} and C_{vs} the specific heats at constant pressure and volume respectively (J/(kg·K)), and κ_s the thermal conductivity (W/(m·K)). The term q represents the power density (W/m^3), applied to the solid material typically via the photothermal or Joule effect. We pinpoint that, throughout the paper, the quantities referring to the liquid and nanotransducer are indexed with 0 and 1, respectively.

We make the following assumptions: (1) the viscous behavior of both the fluid and the solid is neglected, (2) the effect of motion or deformation on heat transfer is neglected within both the fluid and the solid regions, (3) in the solid layer, we assume $C_{ps} = C_{vs}$ and therefore $C_{p1} = C_{ps}$. Hence, the equations for the fluid simplify to

$$\frac{1}{B_0}\frac{\partial p}{\partial t} = \alpha_0\frac{\partial T}{\partial t} - \frac{\partial v}{\partial x},$$
$$\rho_0\frac{\partial v}{\partial t} = -\frac{\partial p}{\partial x},$$
$$\rho_0 C_{p0}\frac{\partial T}{\partial t} = \kappa_0\frac{\partial^2 T}{\partial x^2}, \quad (11)$$

while those of the solid become

$$\frac{1}{B_1}\frac{\partial p}{\partial t} = \alpha_1\frac{\partial T}{\partial t} - \frac{\partial v}{\partial x},$$
$$\rho_1\frac{\partial v}{\partial t} = -\frac{\partial p}{\partial x},$$
$$\rho_1 C_{p1}\frac{\partial T}{\partial t} = \kappa_1\frac{\partial^2 T}{\partial x^2} + q. \quad (12)$$

These equations represent the starting point of our analysis.

In the present work, viscous attenuation in water is neglected. We emphasize that, as the frequency of the acoustic wave increases, acoustic attenuation in the fluid becomes more prominent, therefore at certain frequencies ω (rad/s) of interest in this work, dissipative effects may not be negligible. We observe that the acoustic wave shows an exponential decay within the water in contact with the generating layer, described by an acoustic penetration length $\mathcal{L}_{ac}$ scaling as ω^{-2}. The latter reads

$$\mathcal{L}_{ac} = \frac{2C_0^3}{\omega^2}\frac{1}{\frac{\lambda_0 + 2\mu_0}{\rho_0} + \left(\frac{C_{p0}}{C_{v0}} - 1\right)\frac{\kappa_0}{\rho_0 C_{p0}}}, \quad (13)$$

where all parameters indexed with 0 refer to water, and $C_0 = \sqrt{(B_0/\rho_0)(C_{p0}/C_{v0})}$ is the water sound velocity. This implies that all the following acoustic results are valid only in a water layer that does not exceed $\mathcal{L}_{ac}$. This relation can be easily proved by starting from the set of equations reported in eq 1.[75] We emphasize that the parameters characterizing water behavior can be frequency-dependent, and their high-frequency values are still an open issue. In particular, the viscosities of water are sensibly frequency-dependent in the THz regime, and in this range, the fluid behavior turns out to be non-Newtonian.[83] Moreover, also at the interface between solid and water, the amplitude and phase of the progressive and regressive acoustic waves will be modified by viscosity, since the boundary conditions depend on both the real and imaginary parts of the complex elastic moduli (one simply has to refer to the phasor counterpart of eq 1). For all these reasons, and to explain the physics behind the acoustic generation problem by simple and clear solutions, we neglected viscosity. Nevertheless, we used eq 1 (which considers viscosity and also the effects of mechanical on thermal fields) numerically in some cases and then verified that the transition between thermophone and mechanophone regimes for increasing frequencies turns out to be confirmed for typical viscosity values of water.

Thermal Behavior of the System. The equations in the previous section were formulated in the time domain. Here, we

https://doi.org/10.1021/acs.jpcc.3c01808
J. Phys. Chem. C 2023, 127, 10227−10244

will switch to the frequency domain, where we can solve analytically the equations describing our system. To do so, we assume that the power density is *homogeneously* delivered to the solid layer volume ($x \in [0, L]$) with a sinusoidal time-varying behavior of fixed angular frequency ω: $q(t) = q_\omega e^{i\omega t}$. For ease of notation, from now on we will address q_ω as simply q. Therefore, we can substitute all physical quantities with the corresponding complex-valued phasors and, for the heat equations, we obtain

$$i\omega\rho_1 C_{p1} T = \kappa_1 \frac{\partial^2 T}{\partial x^2} + q, \quad x \in [0, L], \tag{14}$$

$$i\omega\rho_0 C_{p0} T = \kappa_0 \frac{\partial^2 T}{\partial x^2}, \quad x \in [L, +\infty). \tag{15}$$

As for the boundary conditions, at the solid−fluid interface ($x = L$), we set[84−87]

$$T(L^+) - T(L^-) = -rJ(L), \tag{16}$$

$$-\kappa_1 \frac{\partial T}{\partial x}(L^-) = -\kappa_0 \frac{\partial T}{\partial x}(L^+) = J(L), \tag{17}$$

$$-k_1 \frac{\partial T}{\partial x}(0) = J(0) = 0. \tag{18}$$

The quantity $J(x)$ represents the heat flux defined as $J(x) = -\kappa_1 \frac{\partial T}{\partial x}$ in the solid and as $J(x) = -\kappa_0 \frac{\partial T}{\partial x}$ in the fluid, and r ($m^2 \cdot K/W$) is the thermal boundary resistance, or Kapitza resistance, between solid and fluid. The temperature exhibits a jump across the interface, ruled by r, whereas the heat flux remains continuous. The top interface of the solid layer ($x = 0$) is considered adiabatic.

The general solution of eq 14 for $x \in [0, L]$ (nanotransducer) is

$$T(x) = Ae^{\vartheta_1 x} + Be^{-\vartheta_1 x} + \frac{q}{i\omega\rho_1 C_{p1}}, \tag{19}$$

where A and B are unknown coefficients and ϑ_1 is given by

$$\vartheta_1 = \frac{\sqrt{2}}{2}\sqrt{\frac{\omega\rho_1 C_{p1}}{\kappa_1}}(1 + i). \tag{20}$$

On the other hand, the general solution of eq 15 for $x \in [L, +\infty)$ (fluid) is

$$T(x) = Ce^{\vartheta_0 x} + De^{-\vartheta_0 x}, \tag{21}$$

where C and D are unknown coefficients and ϑ_0 is given by

$$\vartheta_0 = \frac{\sqrt{2}}{2}\sqrt{\frac{\omega\rho_0 C_{p0}}{\kappa_0}}(1 + i). \tag{22}$$

We set $C = 0$, since the temperature must remain finite for large values of x. We observe that, while the imaginary part of ϑ_0 corresponds to the propagation constant of the thermal wave, its real part defines the thermal length given by $\mathcal{L}_{th} = 1/\Re e\{\vartheta_0\} = \sqrt{\frac{2\kappa_0}{\omega\rho_0 C_{p0}}}$;[75] i.e., it identifies the penetration length of the thermal wave into the fluid region. Enforcing the boundary conditions stated in eqs 16, 17, and 18 leads to

$$A = B = -\frac{q}{2i\omega\rho_1 C_{p1}} \times \frac{\kappa_0\vartheta_0}{\kappa_0\vartheta_0 \cosh(\vartheta_1 L) + (1 + r\kappa_0\vartheta_0)\kappa_1\vartheta_1 \sinh(\vartheta_1 L)}, \tag{23}$$

$$D = \frac{q}{i\omega\rho_1 C_{p1}} \frac{\kappa_1\vartheta_1 \sinh(\vartheta_1 L)e^{\vartheta_0 L}}{\kappa_0\vartheta_0 \cosh(\vartheta_1 L) + (1 + r\kappa_0\vartheta_0)\kappa_1\vartheta_1 \sinh(\vartheta_1 L)}. \tag{24}$$

We can finally write the solutions for the temperature in both regions as follows. In the solid, $x \in [0, L]$,

$$T(x) = \frac{q}{i\omega\rho_1 C_{p1}} \times \left[1 - \frac{\kappa_0\vartheta_0 \cosh(\vartheta_1 x)}{\kappa_0\vartheta_0 \cosh(\vartheta_1 L) + (1 + r\kappa_0\vartheta_0)\kappa_1\vartheta_1 \sinh(\vartheta_1 L)}\right], \tag{25}$$

and in the fluid, $x \in [L, +\infty)$,

$$T(x) = \frac{q}{i\omega\rho_1 C_{p1}} \times \frac{\kappa_1\vartheta_1 \sinh(\vartheta_1 L)e^{-\vartheta_0(x-L)}}{\kappa_0\vartheta_0 \cosh(\vartheta_1 L) + (1 + r\kappa_0\vartheta_0)\kappa_1\vartheta_1 \sinh(\vartheta_1 L)}. \tag{26}$$

We recall that, to reconstruct the spatiotemporal behavior of a function $f(x, t)$, we must use the complex phasor $f_\omega(x)$ and apply the relation $f(x, t) = \Re e\{f_\omega(x)e^{i\omega t}\}$. In our case, this procedure can be applied to both the temperature T and the heat flux J, where, for ease of notation, the subscript ω has been dropped from the phasors.

Acoustic Behavior of the System. In both solid and fluid regions, the equations for pressure and velocity read, in the frequency domain,

$$\frac{i\omega}{B_{0,1}} p = i\omega\alpha_{0,1} T - \frac{\partial v}{\partial x}, \tag{27}$$

$$i\omega\rho_{0,1} v = -\frac{\partial p}{\partial x}, \tag{28}$$

with subscripts 0 and 1 for the fluid and solid, respectively. This system of equations can be easily rearranged in the more useful form

$$\frac{\omega^2\rho_{0,1}}{B_{0,1}} p + \frac{\partial^2 p}{\partial x^2} = \omega^2\rho_{0,1}\alpha_{0,1} T, \tag{29}$$

$$v = -\frac{1}{i\omega\rho_{0,1}} \frac{\partial p}{\partial x}. \tag{30}$$

Once the first equation is solved for the pressure p, the velocity field v can be directly obtained from the second one. In order to solve the first equation one must consider the temperature profile pertinent to each region, as obtained in the previous section. We now search for the general solution of eq 29, valid for any profile $T(x)$. We start by the homogeneous counterpart of eq 29,

$$\frac{\omega^2\rho_{0,1}}{B_{0,1}} p_h + \frac{\partial^2 p_h}{\partial x^2} = 0, \tag{31}$$

and we directly obtain the solution p_h as

https://doi.org/10.1021/acs.jpcc.3c01808
J. Phys. Chem. C 2023, 127, 10227−10244

$$p_h(x) = Ee^{-\delta_{0,1}x} + Fe^{\delta_{0,1}x}, \tag{32}$$

where

$$\delta_{0,1} = i\omega\sqrt{\frac{\rho_{0,1}}{B_{0,1}}}, \tag{33}$$

and where the constants E and F will be determined through the pertinent boundary conditions. These two terms represent the progressive and regressive pressure waves. Regarding the nonhomogeneous equation,

$$\frac{\omega^2\rho_{0,1}}{B_{0,1}}p_{nh} + \frac{\partial^2 p_{nh}}{\partial x^2} = \omega^2\rho_{0,1}\alpha_{0,1}T, \tag{34}$$

by adopting the method of variation of parameters (Lagrange's method) we can write a particular solution p_{nh} in the form

$$p_{nh}(x) = e(x)p_e(x) + f(x)p_f(x), \tag{35}$$

where $p_e(x) = e^{-\delta_{0,1}x}$ and $p_f(x) = e^{\delta_{0,1}x}$. We remark that eq 35 represents a simple generalization of eq 32 where, however, the coefficients e and f depend on x. Therefore, following Lagrange theory, the first derivatives of e and f fulfill the following algebraic system

$$e'(x)p_e(x) + f'(x)p_f(x) = 0, \tag{36}$$

$$e'(x)p_e'(x) + f'(x)p_f'(x) = \omega^2\rho_{0,1}\alpha_{0,1}T(x), \tag{37}$$

where we used the compact notation $g'(x) = \partial g/\partial x$ for the spatial derivative. This system always has only one solution since the Wronskian determinant $W(x) = p_e(x)p_f'(x) - p_f(x)p_e'(x)$ is different from zero, being given by the explicit relation $W(x) = 2i\omega\sqrt{\rho_{0,1}/B_{0,1}}$. Anyway, the solutions can be easily obtained and read

$$e'(x) = -\frac{1}{2i}\omega\alpha_{0,1}T(x)\sqrt{\rho_{0,1}B_{0,1}}p_f(x), \tag{38}$$

$$f'(x) = \frac{1}{2i}\omega\alpha_{0,1}T(x)\sqrt{\rho_{0,1}B_{0,1}}p_e(x), \tag{39}$$

from which we obtain

$$e(x) = -\frac{1}{2i}\omega\alpha_{0,1}\sqrt{\rho_{0,1}B_{0,1}}\int T(x)e^{\delta_{0,1}x}\,dx, \tag{40}$$

$$f(x) = \frac{1}{2i}\omega\alpha_{0,1}\sqrt{\rho_{0,1}B_{0,1}}\int T(x)e^{-\delta_{0,1}x}\,dx. \tag{41}$$

Finally, the general solution of eq 29, holding on for any temperature profile $T(x)$, can be obtained as the sum of eqs 32 and 35. We eventually obtain

$$p(x) = p_h(x) + p_{nh}(x) = [E + e(x)]e^{-\delta_{0,1}x} + [F + f(x)]e^{\delta_{0,1}x}, \tag{42}$$

where e and f are given in eqs 40 and 41 and are functionals of $T(x)$. We can now specify this general solution for the solid and fluid regions. In the solid region ($x \in [0, L]$), we use the temperature profile given in eq 25 to obtain $e(x)$ and $f(x)$ and, after some straightforward calculations, we obtain

$$p(x) = Ee^{-\delta_1 x} + Fe^{\delta_1 x} + \sqrt{\frac{B_1}{\rho_1}}\frac{\delta_1}{\delta_1^2 - \vartheta_1^2}\frac{\alpha_1 q}{C_{p1}}\left[\frac{\delta_1^2 - \vartheta_1^2}{\delta_1^2} - \frac{\kappa_0\vartheta_0\cosh(\vartheta_1 x)}{\kappa_0\vartheta_0\cosh(\vartheta_1 L) + (1 + r\kappa_0\vartheta_0)\kappa_1\vartheta_1\sinh(\vartheta_1 L)}\right], \tag{43}$$

$$v(x) = \frac{\delta_1}{i\omega\rho_1}Ee^{-\delta_1 x} - \frac{\delta_1}{i\omega\rho_1}Fe^{\delta_1 x} + \sqrt{\frac{B_1}{\rho_1}}\frac{\delta_1}{\delta_1^2 - \vartheta_1^2}\frac{\alpha_1 q}{i\omega\rho_1 C_{p1}} \times \frac{\kappa_0\vartheta_0\vartheta_1\sinh(\vartheta_1 x)}{\kappa_0\vartheta_0\cosh(\vartheta_1 L) + (1 + r\kappa_0\vartheta_0)\kappa_1\vartheta_1\sinh(\vartheta_1 L).} \tag{44}$$

On the other hand, in the fluid region ($x \in [L, +\infty)$) we substitute the temperature profile stated in eq 26, obtaining

$$p(x) = Ge^{-\delta_0 x} + He^{\delta_0 x} + \frac{\rho_0}{\rho_1}\sqrt{\frac{B_0}{\rho_0}}\frac{\delta_0}{\delta_0^2 - \vartheta_0^2}\frac{\alpha_0 q}{C_{p1}}e^{-\vartheta_0(x-L)} \times \frac{\kappa_1\vartheta_1\sinh(\vartheta_1 L)}{\kappa_0\vartheta_0\cosh(\vartheta_1 L) + (1 + r\kappa_0\vartheta_0)\kappa_1\vartheta_1\sinh(\vartheta_1 L)}, \tag{45}$$

$$v(x) = \frac{\delta_0}{i\omega\rho_0}Ge^{-\delta_0 x} - \frac{\delta_0}{i\omega\rho_0}He^{\delta_0 x} + \frac{1}{i\omega\rho_1}\sqrt{\frac{B_0}{\rho_0}}\frac{\delta_0}{\delta_0^2 - \vartheta_0^2}\frac{\alpha_0 q}{C_{p1}}e^{-\vartheta_0(x-L)} \times \frac{\kappa_1\vartheta_1\vartheta_0\sinh(\vartheta_1 L)}{\kappa_0\vartheta_0\cosh(\vartheta_1 L) + (1 + r\kappa_0\vartheta_0)\kappa_1\vartheta_1\sinh(\vartheta_1 L).} \tag{46}$$

In the fluid phase, the coefficients E and F have been substituted with two new symbols G and H to properly distinguish the different regions. We impose $H = 0$ to avoid regressive waves in the fluid (the only acoustic wave comes from the top side of the system).

As for the boundary conditions at the solid liquid-interface we impose[75,81,82]

$$p(L^-) = p(L^+), \tag{47}$$

$$v(L^-) = v(L^+). \tag{48}$$

These relations are equivalent to the continuity of normal mechanical stress and displacement. On the top surface of the nanotransducer ($x = 0$) we have two possibilities describing either the free surface (zero-stress) condition

$$p(0) = 0, \tag{49}$$

or the clamped surface (zero-displacement) condition

$$v(0) = 0. \tag{50}$$

Enforcing the conditions stated in eqs 47 and 48 yields

$$Ee^{-\delta_1 L} + Fe^{\delta_1 L} + \sqrt{\frac{B_1}{\rho_1}}\frac{\delta_1}{\delta_1^2 - \vartheta_1^2}\frac{\alpha_1 q}{C_{p1}} \times \left[\frac{\delta_1^2 - \vartheta_1^2}{\delta_1^2} - \frac{\kappa_0\vartheta_0\cosh(\vartheta_1 L)}{S}\right] = Ge^{-\delta_0 L} + \frac{\rho_0}{\rho_1}\sqrt{\frac{B_0}{\rho_0}}\frac{\delta_0}{\delta_0^2 - \vartheta_0^2}\frac{\alpha_0 q}{C_{p1}}\frac{\kappa_1\vartheta_1\sinh(\vartheta_1 L)}{S}, \tag{51}$$

https://doi.org/10.1021/acs.jpcc.3c01808
J. Phys. Chem. C 2023, 127, 10227−10244

$$\frac{\delta_1}{i\omega\rho_1}Ee^{-\delta_1 L} - \frac{\delta_1}{i\omega\rho_1}Fe^{\delta_1 L} + \sqrt{\frac{B_1}{\rho_1}}\frac{\delta_1}{\delta_1^2 - \vartheta_1^2}\alpha_1 q\frac{\kappa_0\vartheta_0\vartheta_1\sinh(\vartheta_1 L)}{i\omega\rho_1 C_{p1}S} = \frac{\delta_0}{i\omega\rho_0}Ge^{-\delta_0 L} + \sqrt{\frac{B_0}{\rho_0}}\frac{\delta_0\alpha_0 q}{\delta_0^2 - \vartheta_0^2}\frac{\kappa_1\vartheta_1\vartheta_0\sinh(\vartheta_1 L)}{i\omega\rho_1 C_{p1}S}, \tag{52}$$

where

$$S = \kappa_0\vartheta_0\cosh(\vartheta_1 L) + (1 + r\kappa_0\vartheta_0)\kappa_1\vartheta_1\sinh(\vartheta_1 L). \tag{53}$$

The free surface condition for $x = 0$ leads to

$$E + F + \sqrt{\frac{B_1}{\rho_1}}\frac{\delta_1}{\delta_1^2 - \vartheta_1^2}\frac{\alpha_1 q}{C_{p1}}\left[\frac{\delta_1^2 - \vartheta_1^2}{\delta_1^2} - \frac{\kappa_0\vartheta_0}{S}\right] = 0, \tag{54}$$

whereas the clamped surface condition leads to

$$E - F = 0. \tag{55}$$

We introduce a binary parameter b such that $b = +1$ for the free surface condition and $b = -1$ for the clamped surface condition at $x = 0$. Hence, the three boundary conditions (two continuity equations for $x = L$ and one mechanical requirement at $x = 0$) are conveniently cast as follows

$$Ee^{-\delta_1 L} + Fe^{\delta_1 L} = Ge^{-\delta_0 L} + \xi, \tag{56}$$

$$Ee^{-\delta_1 L} - Fe^{\delta_1 L} = \frac{\delta_0\rho_1}{\delta_1\rho_0}Ge^{-\delta_0 L} + \eta, \tag{57}$$

$$E + bF + \frac{1 + b}{2}\varphi = 0, \tag{58}$$

where

$$\xi = \frac{\rho_0}{\rho_1}\sqrt{\frac{B_0}{\rho_0}}\frac{\delta_0}{\delta_0^2 - \vartheta_0^2}\frac{\alpha_0 q}{C_{p1}}\frac{\kappa_1\vartheta_1\sinh(\vartheta_1 L)}{S} - \sqrt{\frac{B_1}{\rho_1}}\frac{\delta_1}{\delta_1^2 - \vartheta_1^2}\frac{\alpha_1 q}{C_{p1}}\left[\frac{\delta_1^2 - \vartheta_1^2}{\delta_1^2} - \frac{\kappa_0\vartheta_0\cosh(\vartheta_1 L)}{S}\right], \tag{59}$$

$$\eta = \sqrt{\frac{B_0}{\rho_0}}\frac{\delta_0}{\delta_0^2 - \vartheta_0^2}\alpha_0 q\frac{\kappa_1\vartheta_1\vartheta_0\sinh(\vartheta_1 L)}{\delta_1 C_{p1}S} - \sqrt{\frac{B_1}{\rho_1}}\frac{\alpha_1 q}{\delta_1^2 - \vartheta_1^2}\frac{\kappa_0\vartheta_0\vartheta_1\sinh(\vartheta_1 L)}{C_{p1}S}, \tag{60}$$

$$\varphi = \sqrt{\frac{B_1}{\rho_1}}\frac{\delta_1}{\delta_1^2 - \vartheta_1^2}\frac{\alpha_1 q}{C_{p1}}\left[\frac{\delta_1^2 - \vartheta_1^2}{\delta_1^2} - \frac{\kappa_0\vartheta_0}{S}\right]. \tag{61}$$

The solution for F can be obtained straightforwardly

$$F = \frac{\frac{\delta_0\rho_1}{\delta_1\rho_0}\xi - \eta + \left(\frac{\delta_0\rho_1}{\delta_1\rho_0} - 1\right)\frac{1 + b}{2}\varphi e^{-\delta_1 L}}{\frac{\delta_0\rho_1}{\delta_1\rho_0}(e^{\delta_1 L} - be^{-\delta_1 L}) + (e^{\delta_1 L} + be^{-\delta_1 L})}, \tag{62}$$

and the other coefficients can be directly calculated through the relations

$$E = -bF - \frac{1 + b}{2}\varphi, \tag{63}$$

$$G = e^{\delta_0 L}\left[F(e^{\delta_1 L} - be^{-\delta_1 L}) - \xi - \frac{1 + b}{2}\varphi e^{-\delta_1 L}\right]. \tag{64}$$

This concludes the determination of the acoustic response of the system with both stress-free ($b = +1$) and zero-displacement ($b = -1$) conditions at the top surface of the solid layer.

Two distinct acoustic wave generation phenomena are predicted from the now-developed model. On the hand, the heat that flows from the solid to the fluid creates compression and dilatation processes in the latter at the same frequency as the applied power density, therein driving acoustic waves. This is the so-called thermophone mechanism. On the other hand, the power density fed to the system also generates an oscillatory strain and stress behavior within the solid, which can thus act as a piston on the fluid, finally generating an acoustic wave in the fluid region, addressed as mechanophone mechanism.[78,79] In order to clarify the interplay and magnitude of these two effects across the frequency spectrum, we calculate the acoustic pressure generated in the two cases by alternatively turning off the thermophone and the mechanophone effects. To turn off the thermophone, we set the water thermal expansion coefficient $\alpha_0 = 0$, and conversely, to turn off the mechanophone we set the solid thermal expansion coefficient $\alpha_1 = 0$. This choice is justified by the fact that the total response of the system is given by the sum of the partial response with $\alpha_0 = 0$ and the partial response with $\alpha_1 = 0$. This is well seen from the mathematical form of the three coefficients in eqs 59, 60, and 61. Indeed, the three coefficients ξ, η, and φ are written as a linear combination of α_0 and α_1.

Purely Mechanophone Acoustic Generation Mechanism. In this first case, we cancel the thermophone effect by suppressing the thermal expansion in the fluid: $\alpha_0 = 0$. The mechanophone thus remains the only generation mechanism. The coefficients entering eqs 59, 60, and 61 reduce to

$$\xi = -\sqrt{\frac{B_1}{\rho_1}}\frac{\delta_1}{\delta_1^2 - \vartheta_1^2}\frac{\alpha_1 q}{C_{p1}}\left[\frac{\delta_1^2 - \vartheta_1^2}{\delta_1^2} - \frac{\kappa_0\vartheta_0\cosh(\vartheta_1 L)}{S}\right], \tag{65}$$

$$\eta = -\sqrt{\frac{B_1}{\rho_1}}\frac{\alpha_1 q}{\delta_1^2 - \vartheta_1^2}\frac{\kappa_0\vartheta_0\vartheta_1\sinh(\vartheta_1 L)}{C_{p1}S}, \tag{66}$$

$$\varphi = \sqrt{\frac{B_1}{\rho_1}}\frac{\delta_1}{\delta_1^2 - \vartheta_1^2}\frac{\alpha_1 q}{C_{p1}}\left[\frac{\delta_1^2 - \vartheta_1^2}{\delta_1^2} - \frac{\kappa_0\vartheta_0}{S}\right]. \tag{67}$$

By means of these coefficients, we can elaborate the expression for the pressure of the acoustic wave in the fluid ($x > L$), obtaining

$$p(x) = -e^{-\delta_0(x - L)} \times \frac{\eta(e^{\delta_1 L} - be^{-\delta_1 L}) + (1 + b)\varphi + \xi(e^{\delta_1 L} + be^{-\delta_1 L})}{\sqrt{\frac{\rho_1 B_1}{\rho_0 B_0}}(e^{\delta_1 L} - be^{-\delta_1 L}) + (e^{\delta_1 L} + be^{-\delta_1 L})}. \tag{68}$$

Now, we separately analyze the cases with $b = +1$ (free surface at $x = 0$) and $b = -1$ (clamped surface at $x = 0$). For $b = +1$, we obtain the following expression for the pressure intensity

https://doi.org/10.1021/acs.jpcc.3c01808
J. Phys. Chem. C 2023, 127, 10227−10244

$$|p| = \left| \frac{\eta \sinh(\delta_1 L) + \varphi + \xi \cosh(\delta_1 L)}{\sqrt{\frac{\rho_1 B_1}{\rho_0 B_0}} \sinh(\delta_1 L) + \cosh(\delta_1 L)} \right| = \left| \frac{\eta i \sin\left(\omega \sqrt{\frac{\rho_1}{B_1}} L\right) + \varphi + \xi \cos\left(\omega \sqrt{\frac{\rho_1}{B_1}} L\right)}{\sqrt{\frac{\rho_1 B_1}{\rho_0 B_0}}\, i \sin\left(\omega \sqrt{\frac{\rho_1}{B_1}} L\right) + \cos\left(\omega \sqrt{\frac{\rho_1}{B_1}} L\right)} \right|, \tag{69}$$

where we used the fact that δ_0 is a purely imaginary number. On the other hand, for $b = -1$, we obtain

$$|p| = \left| \frac{\eta \cosh(\delta_1 L) + \xi \sinh(\delta_1 L)}{\sqrt{\frac{\rho_1 B_1}{\rho_0 B_0}} \cosh(\delta_1 L) + \sinh(\delta_1 L)} \right| = \left| \frac{\eta \cos\left(\omega \sqrt{\frac{\rho_1}{B_1}} L\right) + \xi i \sin\left(\omega \sqrt{\frac{\rho_1}{B_1}} L\right)}{\sqrt{\frac{\rho_1 B_1}{\rho_0 B_0}} \cos\left(\omega \sqrt{\frac{\rho_1}{B_1}} L\right) + i \sin\left(\omega \sqrt{\frac{\rho_1}{B_1}} L\right)} \right|. \tag{70}$$

For small values of the frequency ω, i.e., $\omega \sqrt{\frac{\rho_1}{B_1}} L \ll 1$, we expand to second-order the trigonometric and hyperbolic functions, including those appearing in S, see eq 53. Tedious yet straightforward calculations lead to the following expression for $b = +1$

$$|p| \simeq \frac{q \alpha_1 \rho_1 L^3}{2\sqrt{\rho_0 \kappa_0 C_{p0}}} \omega^{3/2}, \qquad \omega \ll \frac{1}{L} \sqrt{\frac{B_1}{\rho 1}} \tag{71}$$

and, for $b = -1$, to

$$|p| \simeq q \alpha_1 L^2 \sqrt{\frac{\omega B_0}{\kappa_0 C_{p0}}}, \qquad \omega \ll \frac{1}{L} \sqrt{\frac{B_1}{\rho 1.}} \tag{72}$$

This means that, for small values of the frequency, a transducer with a free surface drives a pressure wave in water scaling with $\omega^{3/2}$, whereas for the clamped surface case the scaling is $\omega^{1/2}$. Although in the general case $|p|$ depends on the thermal resistance (S depends on r in previous solutions), for small frequencies this dependence does not appear in eqs 71 and 72. These approximations, for both free and clamped generating layers, will prove useful to find the threshold frequency separating the thermophone and mechanophone contributions.

To conclude, we point out that the mechanophone behavior could be defined by imposing the condition $r \to \infty$. Indeed, in so doing, we prevent heat transfer from the solid to the fluid, eliminating the thermophone effect. In this case, however, we obtain the highest efficiency of the mechanophone mechanism. In fact, if $\alpha_0 = 0$ but r remains finite, we have no thermophone effect but we still have some heat entering the fluid, reducing the energy at disposal for driving mechanical stress oscillations in the solid. Instead, when the resistance r becomes infinite, we eliminate the thermophone effect but we conserve all the energy in the solid, thus maximizing its mechanical oscillations, which in turn drive, by the piston effect, the acoustic wave in the fluid. This analysis is conducted in detail in the Appendix, and it is important both for a better understanding of the system's energetics and to get a clear view of the resonance phenomena observed at high frequencies.

Purely Thermophone Acoustic Generation Mechanism. In this second case, we suppress the mechanophone effect by suppressing the thermal expansion in the solid: $\alpha_1 = 0$. The thermophone thus remains the only generation mechanism. The coefficients entering eqs 59, 60, and 61 reduce to

$$\xi = \frac{\rho_0}{\rho_1} \sqrt{\frac{B_0}{\rho_0}} \frac{\delta_0}{\delta_0^2 - \vartheta_0^2} \frac{\alpha_0 q}{C_{p1}} \frac{\kappa_1 \vartheta_1 \sinh(\vartheta_1 L)}{S}, \tag{73}$$

$$\eta = \sqrt{\frac{B_0}{\rho_0}} \frac{\delta_0}{\delta_0^2 - \vartheta_0^2} \alpha_0 q \frac{\kappa_1 \vartheta_1 \vartheta_0 \sinh(\vartheta_1 L)}{\delta_1 C_{p1} S}, \tag{74}$$

$$\varphi = 0. \tag{75}$$

We obtain the expression for the pressure of the acoustic wave in the fluid ($x > L$) as

$$p(x) = -\mathrm{e}^{-\delta_0 (x-L)} \sqrt{\frac{B_0}{\rho_0}} \frac{\delta_0}{\delta_0^2 - \vartheta_0^2} \frac{\alpha_0 q}{C_{p1}} \frac{\kappa_1 \vartheta_1 \sinh(\vartheta_1 L)}{S} \times \frac{\frac{\theta_0}{i\omega} \frac{B_1}{\rho_1} (\mathrm{e}^{\delta_1 L} - b\mathrm{e}^{-\delta_1 L}) + \frac{\rho_0}{\rho_1} (\mathrm{e}^{\delta_1 L} + b\mathrm{e}^{-\delta_1 L})}{\sqrt{\frac{\rho_1 B_1}{\rho_0 B_0}} (\mathrm{e}^{\delta_1 L} - b\mathrm{e}^{-\delta_1 L}) + (\mathrm{e}^{\delta_1 L} + b\mathrm{e}^{-\delta_1 L})}. \tag{76}$$

In order to further simplify this expression, since for the thermophone mechanism the deformation of the film is not relevant, we can add the additional assumption that $B_1 \to \infty$, which cancels wave propagation in the film and thus all resonance phenomena. This leads to

$$p(x) = -\mathrm{e}^{-\delta_0 (x-L)} \frac{B_0 \delta_0}{\delta_0^2 - \vartheta_0^2} \frac{\alpha_0 \vartheta_0 q}{i\omega \rho_1 C_{p1}} \frac{\kappa_1 \vartheta_1 \sinh(\vartheta_1 L)}{S}, \tag{77}$$

where the parameter b has obviously *disappeared*, since the boundary condition for $x = 0$ no longer has any effect on the undeformable solid. Summarizing, eq 77 is exact under the hypotheses $\alpha_1 = 0$ and $B_1 \to \infty$. The intensity of the pressure of the acoustic wave is then given by

$$|p| = \frac{\alpha_0 \rho_0 q}{\rho_1 C_{p1}} \sqrt{\frac{\omega C_{p0} B_0}{\kappa_0}} \left| \frac{1}{\delta_0^2 - \vartheta_0^2} \frac{\kappa_1 \vartheta_1 \sinh(\vartheta_1 L)}{S} \right|. \tag{78}$$

We analyzed, in the case of the mechanophone, an approximation for the pressure generated at low frequencies since this mechanism is less effective in that portion of the spectrum, see eq 71 or eq 94 for $b = +1$ and eq 72 or eq 98 for $b = -1$. Assuming that, conversely, the thermophone is less effective at high frequencies,[78,79] we now develop, for the pure thermophone case, a valid approximation for intermediate and/or high frequencies. The two approximations will allow us to determine a threshold frequency beyond which the mechanophone mechanism will be more effective than the thermophone. With this aim in mind, we now turn the attention to the term in absolute value in eq 78. For large enough frequencies, the ratio $\kappa_1 \vartheta_1 \sinh(\vartheta_1 L)/S$ can be approximated to $\kappa_1 \vartheta_1 / [\kappa_0 \vartheta_0 + (1 + r\kappa_0 \vartheta_0) \kappa_1 \vartheta_1]$ since $2 \sinh(\vartheta_1 L) \simeq 2 \cosh(\vartheta_1 L) \simeq \exp(\vartheta_1 L)$ for $|\vartheta_1 L| \gg 1$, that is for $\omega \to \infty$. Moreover, if $\mathfrak{Re}\{r\kappa_0 \vartheta_0\} \gg 1$ and $\mathfrak{Re}\{r\kappa_1 \vartheta_1\} \gg 1$, we obtain the simpler relation $\kappa_1 \vartheta_1 \sinh(\vartheta_1 L)/S \simeq 1/(r\kappa_0 \vartheta_0)$. These two further assumptions correspond to $\omega \gg 2/(r^2 \rho_0 \kappa_0 C_{p0})$ and $\omega \gg 2/(r^2 \rho_1 \kappa_1 C_{p1})$, where typically $2/(r^2 \rho_1 \kappa_1 C_{p1}) < 2/(r^2 \rho_0 \kappa_0 C_{p0})$, and therefore, only the first condition is sufficient to justify the

https://doi.org/10.1021/acs.jpcc.3c01808
J. Phys. Chem. C 2023, 127, 10227−10244

approximation. This is especially true if we take gold for the solid film and water for the liquid and if we work in the frequency range of interest for real case scenarios (see the next section for numerical examples). In addition, it is easy to prove that $|1/(\delta_0^2 - \vartheta_0^2)| \simeq \kappa_0/(\omega\rho_0 C_{p0})$ for $\omega \ll B_0 C_{p0}/\kappa_0$. Summing up, these approximations can be applied to eq 78 eventually obtaining

$$|p| = \frac{\sqrt{B_0\rho_0}}{\rho_0 C_{p0}\rho_1 C_{p1}}\frac{\alpha_0 q}{\omega r}, \qquad \frac{2}{r^2\rho_0\kappa_0 C_{p0}} \ll \omega \ll \frac{B_0 C_{p0}}{\kappa_0}. \tag{79}$$

This result shows the degradation of the thermophone effect for increasing ω within the central frequency range, described by a scaling of the pressure intensity $\sim 1/\omega$. For even larger frequency values it is easily seen that the scaling shifts to a faster $1/\omega^2$, a fact that, however interesting, is not relevant to the present analysis.

We remark that for $r \to 0$, the ratio $\kappa_1\vartheta_1 \sinh(\vartheta_1 L)/S$ approximates to $\kappa_1\vartheta_1/[\kappa_0\vartheta_0 + (1 + r\kappa_0\vartheta_0)\kappa_1\vartheta_1]$ but the inequalities $\Re\mathrm{e}\{r\kappa_0\vartheta_0\} \gg 1$ and $\Re\mathrm{e}\{r\kappa_0\vartheta_0\} \gg 1$ no longer hold. Then, from eq 78, the pressure intensity can be approximated with

$$|p| = \frac{\alpha_0 q}{\rho_1 C_{p1}}\sqrt{\frac{k_0 B_0}{\omega C_{p0}}} \times \frac{\sqrt{\rho_1 C_{p1}\kappa_1}}{|\sqrt{\rho_0 C_{p0}\kappa_0} + \sqrt{\rho_1 C_{p1}\kappa_1}(1 + r\kappa_0\vartheta_0)|}, \tag{80}$$

where we have eliminated the singularity for $r = 0$ exhibited by eq 79. In particular, for $r = 0$ (perfect thermophone condition), the approximation reads:

$$|p| = \frac{\alpha_0 q}{\rho_1 C_{p1}}\sqrt{\frac{k_0 B_0}{\omega C_{p0}}}\frac{\sqrt{\rho_1 C_{p1}\kappa_1}}{\sqrt{\rho_0 C_{p0}\kappa_0} + \sqrt{\rho_1 C_{p1}\kappa_1}}, \tag{81}$$

which will be used to prove that, also for $r = 0$, the mechanophone effect can still prevail over the thermophone at high enough frequencies. We remark that, for $r = 0$, the degradation of the thermophone efficiency scales as $1/\sqrt{\omega}$, see eq 81, whereas it scales as $1/\omega$ for sufficiently large values of r, see eq 79. We thus conclude that increasing the Kapitza resistance from zero to a sufficiently high value not only degrades the thermoacoustic performance but also changes the shape of the pressure wave frequency dependence.

RESULTS AND DISCUSSION

We here compare the magnitude of mechanophone and thermophone mechanisms by identifying the threshold frequency corresponding to the predominance of one of the two effects. Moreover, we discuss a pulsed excitation scenario within a time-domain perspective.

Relative Magnitude of Mechanophone and Thermophone Mechanisms. For the sake of calculations, we contextualize the previous results for the case of a gold film, $L = 20$ nm, in contact with water. We take the following material-dependent parameters: $\rho_0 = 10^3$ kg/m^3, $B_0 = 2.15 \times 10^9$ Pa, $\alpha_0 = 3.03 \times 10^{-4}$ 1/K, $C_{p0} = 4.4 \times 10^3$ J/(kg·K), and $\kappa_0 = 6.07 \times 10^{-1}$ W/(m·K) for water and $\rho_s = 19.32 \times 10^3$ kg/m^3, $\mu_s = 27 \times 10^9$ Pa, $\lambda_s = 160 \times 10^9$ Pa, $\alpha_s = 42 \times 10^{-6}$ 1/K, $C_{ps} = 130$ J/(kg·K), and $\kappa_s = 310$ W/(m·K) for gold. These parameters can be found in the literature, for example in refs 55, 88, and 89. The 20 nm thick gold film, for the clamped surface case, can be deposited over a rigid substrate made out of a material with an acoustic impedance higher than Au and functionalized so as to obtain a Kapitza resistance with Au exceeding that at the Au-water interface. This can be achieved via plasma-enhanced chemical vapor deposition (PECVD) or other sputtering techniques. This sample may then be covered/immersed in water. On the other hand, the free surface case can be realized by chemically synthesizing gold nanoplatelets and drop casting them on the water surface.[90−92] Although these methods may change the parameters slightly from those of bulk material, we use standard values here, as the results only serve to delineate the underlying physics. Regarding the thermal boundary resistance, we assume $r = 3 \times 10^{-8}$ m^{2}K/W, a realistic value for the gold/water interface.[93] In the following, we also consider the ideal case with zero thermal resistance and a case with a larger resistance $r = 3 \times 10^{-7}$ m^{2}K/W; the latter can be possibly achieved through interface functionalization,[80] e.g., with a graphene coating.[94] Figures 2 and 3 report the frequency spectrum of the pressure

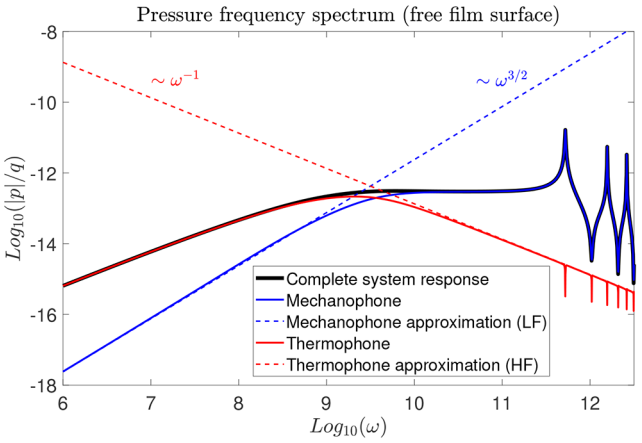

Figure 2. Water pressure intensity frequency spectrum for the case of gold free film surface at $x = 0$ ($b = +1$) and $r = 3 \times 10^{-8}$ m^{2}K/W. The total pressure (eq 45 specialised for $b = +1$, black curve) is compared to the sole mechanophone contribution (eq 69, blue curve) and sole thermophone contribution (eq 76, red curve). Moreover, the low-frequency approximation of the sole mechanophone response (eq 71, blue dashed line) and the high-frequency approximation of the sole thermophone response (eq 79, red dashed line) are reported. The intersection of the two approximated curves identifies the threshold frequency beyond which the mechanophone mechanism becomes predominant.

generated in water for the case of the free gold film surface (i.e., $b = +1$) and for that of a clamped surface (i.e., $b = -1$), respectively. The curves are normalized with respect to the power density q absorbed by the gold film. These spectra show that the thermophone is predominant at low frequencies, while the mechanophone prevails at high frequencies. Indeed, in these figures, we compare the complete solution for the total pressure ($\alpha_0 \neq 0$ and $\alpha_1 \neq 0$, black line) given by eq 45 with the purely mechanophone solution ($\alpha_0 = 0$, blue line) given in eq 69 (with $b = +1$) or eq 70 (with $b = -1$) and the purely thermophone solution ($\alpha_1 = 0$, red line) given in eq 76 (with $b = \pm 1$). The thermophone contribution clearly overlaps the total pressure for low values of ω, while for large ω values the mechanophone becomes the only significant contribution, overlapping the total pressure. In both figures, in the high-frequency range, the mechanophone effect and, as a consequence, the total pressure, show very prominent upward and downward peaks. These are

https://doi.org/10.1021/acs.jpcc.3c01808
J. Phys. Chem. C 2023, 127, 10227−10244

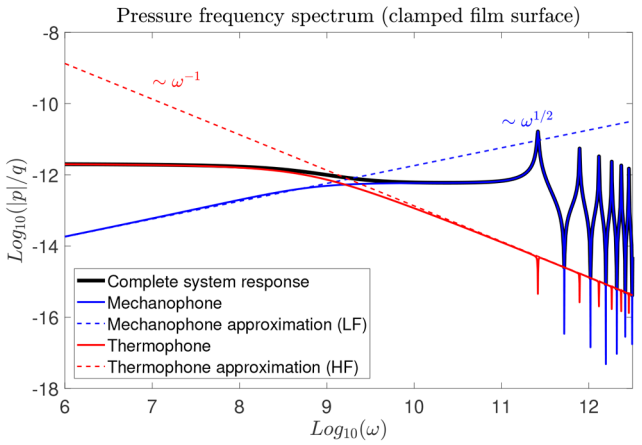

Figure 3. Water pressure intensity frequency spectrum for the case of gold clamped film surface at $x = 0$ ($b = -1$) and $r = 3 \times 10^{-8}$ m^{2}K/W. The total pressure (eq 45 specialised for $b = -1$, black curve) is compared to the sole mechanophone contribution (eq 70, blue curve) and sole thermophone contribution (eq 76, red curve). Moreover, the low-frequency approximation of the sole mechanophone response (eq 72, blue dashed line) and the high-frequency approximation of the sole thermophone response (eq 79, red dashed line) are reported. The intersection of the two curves from the approximations identifies the threshold frequency beyond which the mechanophone mechanism becomes predominant.

due to the activation of the film's vibrational modes, resulting in resonances (upward peaks) and anti-resonances (downward peaks). The peaks, in Figure 2, correspond to the acoustic eigenfrequencies of a free-standing Au film: $\omega_n = \pi v_L n/L$, where $v_L = \sqrt{\frac{B_1}{\rho_1}} = \sqrt{\frac{\lambda_s + 2\mu_s}{\rho_s}}$ is the sound longitudinal velocity; see eq 9, and $n = 1, 2, 3, ...$, etc. Specifically, the resonances (upward peaks) frequencies correspond to the eigenmodes with odd n, whereas antiresonances (downward peaks) correspond to the eigenmodes with even n (see Appendix). This is due to the fact that the source term q in the last line of eq 2 is *spatially homogeneous*, ultimately resulting in a *spatially homogeneous* mechanical excitation of the film. We remark that, for thicker films, the heating can be inhomogeneous, and so this behavior can be significantly altered.[95] Also the purely thermophone case presents downward peaks at the same odd n frequencies, despite the nanofilm thermal expansion being zero in this case. This is due to the expansion and compression of water which, in the thermophone effect, pushes against the nanofilm activating its eigenfrequencies, specularly to what happens during the mechanophone effect. We emphasize that we only observe antiresonances because mechanical energy can only transit from the fluid to the solid, hence leading to a pressure reduction in the liquid itself. We also remark that the formula for the high-frequency thermophone approximation, see eq 79, doesn't show any peak. This is due to the gold bulk modulus approximation $B_1 \to \infty$, which we implemented for extracting eq 79, which implies an incompressible nanofilm. Finally, we notice that the pressure presents different resonance frequencies in the case of a free film surface (as in Figure 2) and in that of the clamped film surface (as in Figure 3). This is consistent with the free−free and free-clamped film's breathing modes[96] (see Appendix).

Threshold Frequency. Returning to the thermophone and mechanophone contributions, the curves corresponding to these two effects intersect for a given frequency, corresponding to the threshold for the predominance of one of the two effects. Nonetheless, from the mathematical point of view, it is challenging to find a simple analytical expression for the threshold frequency by looking for intersections between the two curves related to mechanophone (blue curve) and thermophone (red curve) effects. However, it turns out to be rather easy to find, in straightforward analytical terms, the intersection between the approximated pressure curves, plotted in Figure 2, for both the mechanophone (blue dashed curve) and thermophone (red dashed curve) mechanisms, respectively. To this end, for the free surface case ($b = +1$, Figure 2), we calculate the intersection point between the low frequency (LF) approximation of the mechanophone, given in eq 71, and the high frequency (HF) approximation of the thermophone, in eq 79. The frequency threshold turns out to be

$$\omega^*(b = +1) = \left[2\frac{\alpha_0}{\alpha_1}\frac{1}{r\rho_1^2 C_{p1} L^3}\sqrt{\frac{B_0\kappa_0}{C_{p0}}}\right]^{2/5}. \tag{82}$$

It represents the frequency beyond which the mechanophone prevails for the case of a free surface at $x = 0$, as can be appreciated from Figure 2. For the clamped surface case ($b = -1$, Figure 3), we follow the same reasoning, intersecting the curves pertaining to the low frequency (LF) approximation of the mechanophone response eq 72 with that of the high frequency (HF) approximation of the thermophone response eq 79. For the frequency threshold we obtain

$$\omega^*(b = -1) = \left[\frac{\alpha_0}{\alpha_1}\frac{1}{r\rho_1 C_{p1} L^2}\sqrt{\frac{\kappa_0}{\rho_0 C_{p0}}}\right]^{2/3}, \tag{83}$$

that represents the frequency beyond which the mechanophone prevails for the case of a clamped surface at $x = 0$, as can be appreciated from Figure 3.

Equations 82 and 83 for the threshold frequencies are valid only for finite values of the thermal boundary resistance. In the case of $r \to 0$, the threshold values are obtained by adopting eq 80 instead of eq 79. Also for this case, we consider both the cases $b = +1$ and $b = -1$. When $b = +1$ (free surface at $x = 0$), we intersect the curves given by eq 81 and eq 71, obtaining:

$$\omega^*(b = +1, r = 0) = \left[2\frac{\alpha_0}{\alpha_1}\frac{1}{\rho_1^2 C_{p1} L^3}\kappa_0\sqrt{B_0\rho_0} \times \frac{\sqrt{\rho_1 C_{p1}\kappa_1}}{\sqrt{\rho_0 C_{p0}\kappa_0} + \sqrt{\rho_1 C_{p1}\kappa_1}}\right]^{1/2}. \tag{84}$$

On the other hand, when $b = -1$ (clamped surface at $x = 0$), we intersect the curves given by eq 81 and eq 72, this time yielding

$$\omega^*(b = -1, r = 0) = \frac{\alpha_0}{\alpha_1}\frac{1}{\rho_1 C_{p1} L^2}\kappa_0 \times \frac{\sqrt{\rho_1 C_{p1}\kappa_1}}{\sqrt{\rho_0 C_{p0}\kappa_0} + \sqrt{\rho_1 C_{p1}\kappa_1}}. \tag{85}$$

These results show that even in the most unfavorable conditions for the mechanophone, i.e. where the thermal boundary resistance is negligible, there still exists a threshold frequency, beyond which the mechanophone mechanism turns out to be predominant over the thermophone.

https://doi.org/10.1021/acs.jpcc.3c01808
J. Phys. Chem. C 2023, 127, 10227−10244

We now give an intuitive physical interpretation of these results. To this end, eqs 82 and 83 are conveniently cast in the forms:

$$\omega^*(b=+1)=\left[\frac{\alpha_0}{\alpha_1}\frac{1}{\tau_1\tau_0^{1/2}}\frac{2}{L}\frac{\rho_0}{\rho_1}\sqrt{\frac{B_0}{\rho_0}}\right]^{2/5}, \tag{86}$$

and

$$\omega^*(b=-1)=\left[\frac{\alpha_0}{\alpha_1}\frac{1}{\tau_1\tau_0^{1/2}}\right]^{2/3}, \tag{87}$$

with $\tau_1 = r\rho_1 C_{p1} L$, $\tau_0 = r_0\rho_0 C_{p0} L$ and $r_0 = (\kappa_0/L)^{-1}$. The quantity τ_1 yields an estimate of the film's cooling time. Specifically, the temperature time evolution of a hot film's cooling follows a single exponential decay with a time constant τ_1, provided that the Biot number satisfies $Bi = (L/\kappa_1)/r \ll 1$, and the surrounding environment (water) remains isothermal during the film's cooling process. Similarly, τ_0 is the exponential cooling time of a warm water slab of thickness L, i.e., with the same dimensions as the Au film, in contact, on one side, with a colder isothermal water environment. In the latter scheme, (i) the water's slab temperature is assumed spatially homogeneous during the cooling process, and (ii) the Fourier equation throughout the slab is substituted by a Kapitza resistance boundary condition at the interface between the warm water slab and the cold isothermal water in contact with it. The introduced Kapitza resistance is therefore $r_0 = (\kappa/L)^{-1}$. The cooling time of a slab is the same as the warming time of the same slab in contact with an isothermal hot reservoir; with this respect, the situation may be seen as very similar to the charging and discharging dynamics of a capacitor in an electrical circuit. It is thus convenient to look at the system as a gold film in contact with a water slab of the same thickness under the above-mentioned lumped-model assumptions.

Within this lumped-elements viewpoint, the physics ruling $\omega^*(b=\pm1)$ stems out rather intuitively. The ratio α_0/α_1 implies that the thermophone dominates for all frequencies, i.e., $\omega^*(b=\pm1)\to\infty$, if the thermal expansion of the liquid is much greater than that of the film. Vice versa, the mechanophone effect always dominates, i.e. $\omega^*(b=\pm1)\to 0$, if the thermal expansion of the film far exceeds that of the liquid. Let us now comment on the physics behind the fact that $\omega^*(b=\pm1)$ is a monotonously decreasing function of τ_1 and τ_0. For the sake of clarity, we address limiting case scenarios. As for τ_1, in a situation where the metal film is thermally decoupled from the liquid (i.e. $r\to\infty$), the film's cooling time $\tau_1\to\infty$, hence eqs 86 and 87 show that the mechanophone is the dominant contributing term at all frequencies. This is consistent with the following intuitive physical picture: heat transfer to the liquid is here impeded; hence, water expansion cannot effectively occur, and only the mechanophone contributes to generating the acoustic wave in water. On the contrary, when the thermal coupling between the metal film and the liquid approaches the perfect case (i.e., $r\to 0$), the film's cooling time $\tau_1\to 0$, hence eqs 86 and 87 show that the thermophone is the dominant effect at all frequencies. In such a scenario, heat transfer to the liquid is maximum and the mechanophone contribution is expected to diminish. As for τ_0, in a situation where the liquid slab heating time $\tau_0\to\infty$ (for instance because of a very low liquid thermal diffusivity $D_0 = \kappa_0/(\rho_0 C_{p0})$), eqs 86 and 87 show that the mechanophone dominates at all frequencies. This is consistent with the fact that, in such conditions, the water's slab temperature remains constant, hence water expansion cannot take place. The contrary holds when $\tau_0\to 0$ (very high liquid thermal diffusivity).

Noticeably, only $\omega^*(b=+1)$ is a monotonously increasing function of the liquid bulk modulus B_0, whereas $\omega^*(b=-1)$ does not depend on it. These results may be intuitively grasped as follows. The metallic film undergoes a thermal expansion ΔL. For $b=-1$ (clamped surface), the metallic film has zero displacement at its top surface ($x=0$); hence, the maximum displacement, ΔL, occurs at the film−liquid boundary ($x=L$). Continuity of the displacement field thus leads to the same expansion on the liquid side of the boundary regardless of B_0 (we recall that the results are obtained under the constraint that the thermal response affects the mechanical one but not vice versa: expansion does not imply a temperature change). Otherwise stated, the piston effect, provided by the film pressing on the liquid, is independent of B_0, and so is the frequency threshold. On the contrary, for $b=+1$, at $x=0$ the film surface is free. This implies that the film thermal expansion leads to a non-zero displacement both at $x=0$ and $x=L$. Let's start with the limit case $B_0\to 0$: the metallic film would be free-standing, and the displacement field would have the same absolute value, $\Delta L/2$, but an opposite sign at the two boundaries. As B_0 increases, the displacement absolute value diminishes at $x=L$ and augments at $x=0$, until it reaches the value ΔL at $x=0$ and a null value at the $x=L$ interface for $B_0\to\infty$. Continuity of the displacement field across the $x=L$ interface implies that the expansion of the liquid in contact with the interface decreases with continuity from $\Delta L/2$ to zero as B_0 grows from zero to large values. Therefore, the mechanophone contribution (piston effect) is a monotonously decreasing function of B_0. This explains why $\omega^*(b=+1)\to\infty$ as $B_0\to\infty$, i.e. the mechanophone contribution is not present for high enough values of B_0. Similar arguments can also be developed for eqs 84 and 85.

Kapitza resistance. A comparison of different thermal boundary resistances values in the thermophone vs mechanophone competition, in the frequency domain, is reported in Figure 4, where we show the pressure vs frequency curve (same colors as for Figure 2) for $r=0$ and 3×10^{-7} m^{2}K/W. Figure 4 and Figure 5 show results for the free ($b=+1$) and clamped ($b=$

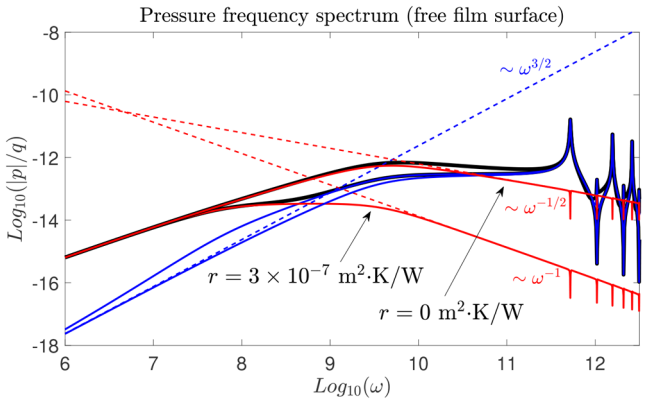

Figure 4. Effect of the thermal boundary resistance on the pressure intensity frequency spectrum with film surface free at $x=0$ ($b=+1$). The physical parameters and color codes are the same as for the curves in Figures 2 and 3, except the values of r, which are shown in the figure. The approximated high-frequency response of the thermophone with $r=0$ is obtained from eq 81, and for $r>0$ from eq 79. The thermophone response scales as $\sim 1/\omega$ for $r>0$, and as $1/\sqrt{\omega}$ for $r=0$.

https://doi.org/10.1021/acs.jpcc.3c01808
J. Phys. Chem. C 2023, 127, 10227−10244

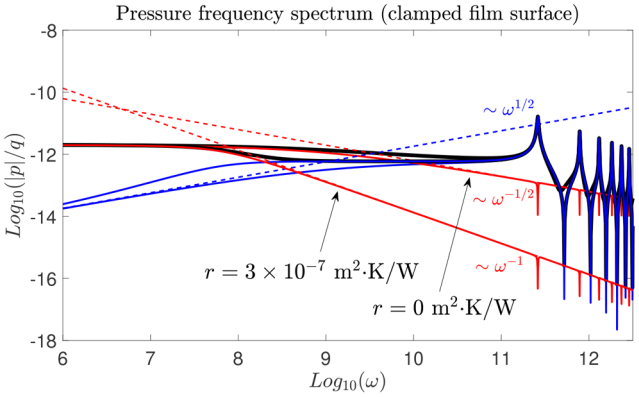

Figure 5. Effect of the thermal boundary resistance on the pressure intensity frequency spectrum with film surface clamped at $x = 0$ ($b = -1$). The physical parameters and color codes are the same as for the curves in Figures 2 and 3, except for the values of r, which are shown in the figure. The approximated high-frequency response of the thermophone with $r = 0$ is obtained from eq 81. The thermophone response scales as $\sim 1/\omega$ for $r > 0$, and as $1/\sqrt{\omega}$ for $r = 0$.

-1) surfaces, respectively. In both cases, as the thermal boundary resistance decreases, the thermophone contribution is effective over a broader frequency range, with the threshold frequency, above which the mechanophone prevails, shifting towards higher frequencies. From a practical standpoint, therefore, the mechanophone effect at high frequencies is particularly important in systems where the thermal boundary resistance is sufficiently high. In addition, in Figure 4, we can appreciate that the degradation of the efficiency of the thermophone mechanism follows a $1/\omega$ law when r is sufficiently high, in accordance with eq 79, and instead scales as $1/\sqrt{\omega}$ when r is exactly zero, as predicted from eq 81. However, despite the higher slope of degradation of the thermophone mechanism in the case of $r > 0$, mechanophone compensation extends the efficiency of the total pressure to a significantly wider frequency range.

We now compare some of asymptotic behaviors of the sound pressure level, for low and high values of ω, with results from the literature. We consider the free film surface results (as shown, e.g., in Figure 4). It can be deduced, via a thorough analysis, that, in the low-frequency range, the thermophone pressure always falls between two asymptotic bounds scaling as $\sqrt{\omega}$ and ω, respectively, the actual behavior depending on the thermal parameters and geometry of the system.[65,66] Indeed, the ideal behavior, scaling as ω in the low-frequency range, is considered as the ultimate limit for the thermoacoustic efficiency.[29,42,69] The high-frequency thermophone regime (whose scaling law varies from $1/\omega$ to $1/\sqrt{\omega}$, depending on r) is less studied in the literature since it is not useful for most applications. However, the thermophone asymptotic behavior for large ω can be found, e.g., in refs 75 and 77, where the near-field sound pressure level is investigated over a wide frequency range. Unfortunately, no comparison is possible for the mechanophone case, for each thermal boundary resistance value. To the authors' knowledge, the asymptotic behaviors in such cases are presented here for the first time.

Pulsed Excitation Scenario: A Time-Domain Perspective. The frequency sweep analysis, performed in previous sections, is very instructive from a fundamental standpoint. It yields plain and handy formulas, allowing to inspect how the interplay of the thermal parameters and excitation frequency affect the generation mechanism and the crossover from the thermophone to mechanophone regime. Excitation with time-harmonic sources, covering the frequency range so far explored, is though unrealistic in a true experimental scenario, where the exploited source would rather be a pulsed laser delivering gaussian laser pulses of duration τ. For instance, in the case of the Au nanofilm on water, with $r = 3 \times 10^{-8}$ m^{2}K/W, the mechanophone becomes predominant for angular frequencies beyond the GHz range; see Figure 4. Such a wide acoustic bandwidth (BW) is excitable for example with a laser pulse with $\tau = 50$ ps, i.e., BW $\sim 1/\tau \sim 20$ GHz.

The question then arises whether the handy and insightful frequency-sweep analysis remains a good predictive tool also for the photoacoustic problem triggered by a pulsed laser source. At first glance, the answer might appear affirmative. As a matter of fact, a pulsed laser excitation may be seen in Fourier space as a sum of time-harmonic sources, covering the angular frequency range from 0 Hz to $\sim\tau^{-1}$. Nevertheless, this needs to be proved since, a priori, there is a difference between exciting the system with a single frequency ω or with all frequencies *up to* the frequency ω. With this aim in mind, we now investigate the same gold film/water system, but under impulsive excitation as opposed to a time-harmonic one. Let us, therefore, proceed to illustrate the time-domain perspective.

For the sake of brevity, we only address the case of the Au film of thickness 20 nm with free boundary conditions at $x = 0$ ($b = +1$). This system closely resembles the Au nanoplate-on-water sample experimentally addressed in the seminal paper in ref 90 under pulsed laser excitation.

The opto-thermo-acoustic dynamics of the system occurs via the following steps: (i) initially the system is at equilibrium at a uniform temperature T_0; (ii) a light pulse strikes the system and delivers energy to the gold nanofilm; (iii) the nanofilm converts the absorbed energy into heat, raising its temperature and exchanging heat with the water region through the Kapitza resistance; (iv) both the nanofilm and water expand, launching acoustic waves in water via the mechanophone and thermophone effects. As for the modeling, we address the problem in the time domain. Specifically, the thermal dynamics is described by eq 12 (last line) for the nanofilm and eq 11 (last line) for water. The acoustic response is accounted for through eq 12 (first and second lines) for the nanofilm, and eq 11 (first and second lines) for water. Also, the boundary conditions remain unaltered. The only difference concerns the source term q entering the third line of eq 12, which is now a pulse in time rather than being harmonic. The laser pulse intensity (W/m^2) has gaussian temporal dependence:

$$I(t) = 2\sqrt{\frac{\ln(2)}{\pi}}\frac{\Phi}{\tau}\exp\left(-4\ln(2)\frac{(t-t_0)^2}{\tau^2}\right), \tag{88}$$

where τ is the pulse temporal full width at half maximum (FWHM), t_0 is the time at which the pulse temporal peak occurs, and Φ is the laser fluence (J/m^2). In our simulations, we will explore different τ values, while Φ will always be kept constant ($\approx$7.5 J/m^2, a typical value used in experiments) for the sake of comparison. We do not consider here the femtosecond regime, where the metal electrons and lattice are out of equilibrium upon laser absorption.[97]

We chose the laser wavelength $\lambda_p = 550$ nm, a value typically used in bio-photoacoustics applications. The latter falls in the visible range and within the water transparency window. We can therefore assume absorption to be negligible in water, while

https://doi.org/10.1021/acs.jpcc.3c01808
J. Phys. Chem. C 2023, 127, 10227−10244

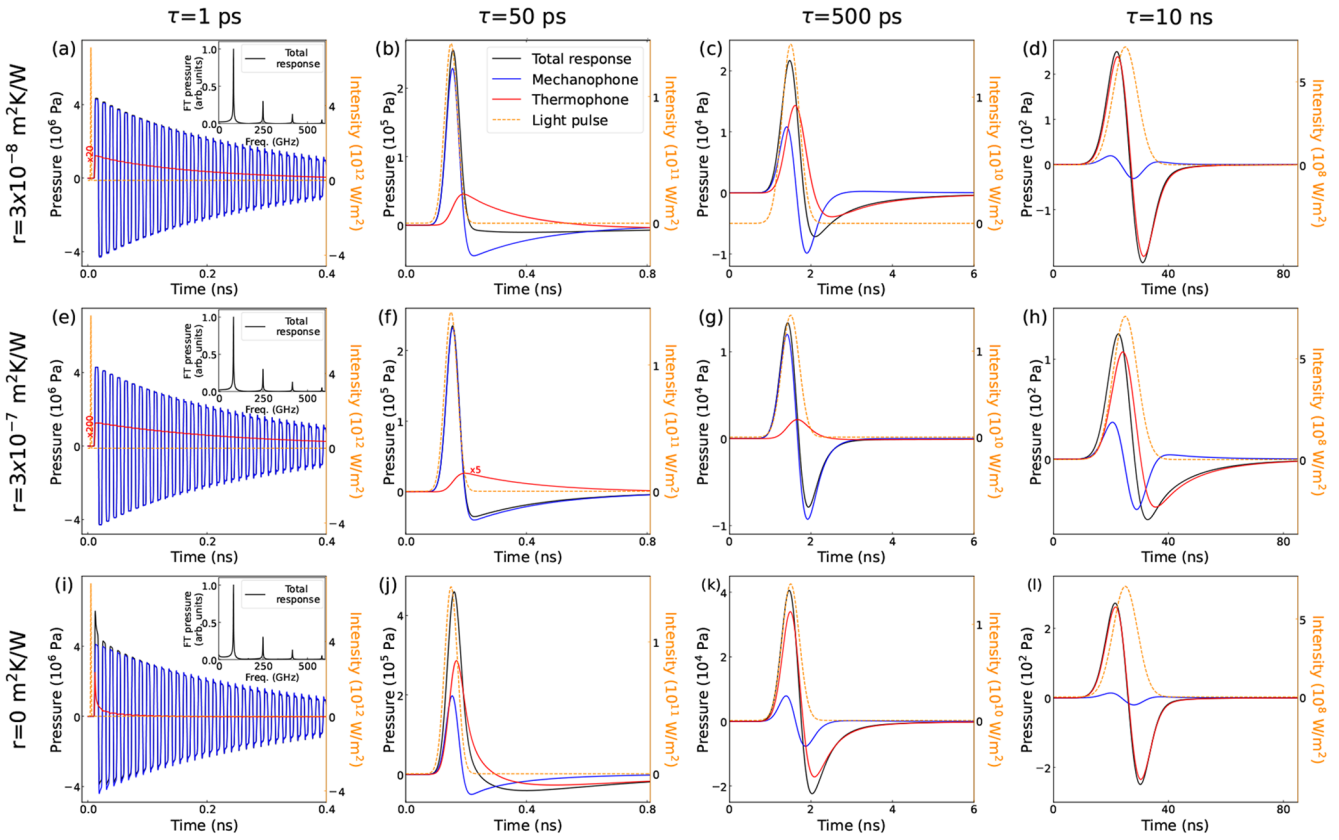

Figure 6. Time evolution of the pressure field for varying Kapitza resistances r (row) and pulse durations τ (columns) for the case of the gold free film surface at $x = 0$ ($b = +1$). We adopted $r = 3 \times 10^{-8}$ m^{2}K/W in panels a−d, $r = 3 \times 10^{-7}$ m^{2}K/W in panels e−h, and $r = 0$ m^{2}K/W in panels i−l. Left axis: pressure in water 10 nm from the nanofilm/water interface, total pressure (black curves), thermophone pressure contribution (red curves) and mechanophone pressure contribution (blue curves). Right axis: light pulse intensity (orange dashed line). The light pulse intensity maximum occurs at the time instant t_0. The scales differ in each panel. Insets in panels of column 1: modulus of FT of the total pressure. The thermophone pressure contributions (red curves) have been multiplied by a factor of 20 in panel a, 200 in panel e, and 5 in panel f, for ease of visibility.

being effective only within the Au film. The refraction index (defined by its real, n, and imaginary, κ, parts) at 550 nm is $n = 1$ for air, $n = 0.39$ and $\kappa = 2.48$ for the gold film,[98] and $n = 1.33$ for water.[99] With these values, we calculate an absorption coefficient $A = 0.18$ for the air/20 nm gold film/water multi-layer.[100] Furthermore, given the exiguous film thickness (also matching the light penetration depth in Au), hot electrons contribute to homogenizing the absorbed power density q throughout the film[101,102] on a time scale shorter than the mechanical and thermal dynamic time scales involved in the launching of the pressure wave in water. We remark that the penetration depth here reported, matching the film thickness, is calculated for the case of a semi-infinite Au region. It is here mentioned just because it is often used as a handy figure of merit. However, the actual absorption coefficient $A = 0.18$ has been calculated by solving the electromagnetic problem for the realistic air/20 nm gold film/water multi-layer, yielding a spatially flattened energy deposition within the film depth (eventually corresponding to a larger penetration depth). In summary, the source term q is here assumed spatially homogeneous and reads $q(t) = AI(t)/L$. The equations are then solved numerically via Finite Element Methods.

We now discuss simulation results for the impulsive excitation scheme. First of all, we need to identify the values of τ to be adopted for a meaningful comparison with the frequency-domain study. With reference to Figure 2, for $r = 3 \times 10^{-8}$ m^{2}K/W, the frequency domain is suitably partitioned into four spectral regions: (1) low-frequency range ($\omega \leq 10^8$ rad/s), where the thermophone contribution prevails; (2) intermediate-range close to the frequency threshold ($\omega \approx 3 \times 10^9$ rad/s), where the thermophone and mechanophone contribute similarly; (3) high-frequency range ($\omega \approx 3 \times 10^{10}$ rad/s), where the mechanophone is predominant; and (4) very high-frequency range ($\omega \geq 5 \times 10^{11}$ rad/s), where the mechanophone is predominant and the nanofilm oscillations are activated. To access these spectral regions, we need to excite the system with a light pulse of duration $\tau \approx 1/\omega$, with ω={10^8, 3×10^9, 3×10^{10}, 5×10^{11}} rad/s. This approximately corresponds to $\tau = 10$ ns, 500 ps, 50 ps, and 1 ps. We underline once more that the laser pulse potentially excites *all frequencies up to* $1/\tau$, that is, within its bandwidth.

Figure 6 shows the time evolution of the pressure in the water, 10 nm from the nanofilm/water interface, for the above-mentioned τ values (columns) and for the Kapitza resistances r addressed so far (rows). In each panel, the total pressure (black curve) is reported together with the thermophone (red curve) and the mechanophone (blue curve) contributions. The laser pulse intensity profile, $I(t)$, is also reported (orange dashed line, right axis). We analyze the results row by row, that is fixing the Kapitza resistance value and increasing the light pulse duration (moving across different columns).

Let's start with the first row, i.e. $r = 3 \times 10^{-8}$ m^{2}K/W. Panel a corresponds to $\tau = 1$ ps; hence, the BW includes all frequencies up to the "very high frequency" range. The mechanophone effect

https://doi.org/10.1021/acs.jpcc.3c01808
J. Phys. Chem. C 2023, 127, 10227−10244

outperforms the thermophone (note that for visualization purposes the thermophone contribution has been amplified by a factor of 20). Moreover, such a short light pulse triggers resonances of the nanofilm, thus resulting in water pressure oscillations, as appreciated from the inset of panel a, where the magnitude of the Fourier transform (FT) of the total pressure is reported in arbitrary units. The frequencies resonances match those reported in Figure 2 (odd n eigenmodes of the film), whereas the FT spectrum correctly shows exactly zero contributions from the frequencies corresponding to the antiresonances in Figure 2 (FT spectra are in linear scale instead of logarithmic scale). Moving to $\tau = 50$ ps in panel b, the BW includes all frequencies up to the "high frequency" range, and again the main contribution is provided by the mechanophone effect. In this case, though, the frequency BW does not extend far enough to activate the film's acoustic eigenmodes. The situation changes in panel c, where $\tau = 500$ ps implies a BW reaching up to the threshold frequency ($\omega \approx 3 \times 10^9$ rad/s, see Figure 2). In this case, the thermophone and the mechanophone have very similar amplitudes, the total pressure being generated from both mechanisms. Finally, the thermophone prevails over the mechanophone for $\tau = 10$ ns in panel d, where the light pulse BW overlaps only the "low frequency" region. Summarizing, for the case of $r = 3 \times 10^{-8}$ m^{2}K/W, the salient features match the predictions of the frequency-sweep analysis.

We now explore the role of Kapitza resistance in the frame of the pulsed excitation scheme. The discussion is always with reference to Figure 6 (now, second row with $r = 3 \times 10^{-7}$ m^{2}K/W). For an increased r value, the frequency threshold is shifted towards smaller frequencies. This can be seen in panel g, where the mechanophone contribution exceeds by far the thermophone one. This is in contrast to what happens for $r = 3 \times 10^{-8}$ m^{2}K/W in panel c, where, for the same $\tau = 500$ ps, the thermophone and mechanophone contributions are comparable. The fact that the mechanophone prevails at high Kapitza resistances is appreciated also for $\tau = 1$ ps in panel e, and for $\tau = 50$ ps in panel f. For the sake of visualization, we had to multiply the thermophone contributions by a factors of 200 in panel e, and of 5 in panel f. For $\tau = 10$ ns in panel h, corresponding to the low-frequency region, the thermophone contribution exceeds the mechanophone one, but to a lesser extent than for the $r = 3 \times 10^{-8}$ m^{2}K/W case in panel d.

We now turn to the case with $r = 0$ m^{2}K/W (third row). The result with $\tau = 50$ ps in panel j demonstrates the threshold frequency shifts towards higher values for a vanishing Kapitza resistance. Indeed, the thermophone contribution is higher than the mechanophone one, at variance with the finite Kapitza resistances cases discussed in the previous figure's rows, where the major contribution was provided by the mechanophone. The dominance of the thermophone is, of course, even more remarkable for $\tau = 500$ ps in panel k, and for $\tau = 10$ ns in panel l. Nevertheless, the case with $\tau = 1$ ps in panel i shows a prevailing mechanophone contribution. This result demonstrates that, even in the case of an impulsive excitation, there is a frequency threshold above which the mechanophone prevails even in the worst-case scenario of a vanishing Kapitza resistance.

CONCLUSIONS

We developed a fully analytical model describing acoustic wave generation in a fluid triggered by a solid nanometric film, i.e., the nanostransducer, upon absorption of a sinusoidal time-dependent power density. Two generation mechanisms are evidenced: the thermophone and the mechanophone. In the former, the nanotransducer plays the role of a nano-heater, harmonically heating the proximal liquid. The resulting time-harmonic thermal expansion of the liquid ultimately drives the pressure wave in the liquid itself. In the latter, it is the sinusoidal thermal expansion of the nanotransducer, directly acting as a mechanical piston on the surrounding liquid, that drives the pressure wave. We recognize the relevant physical parameters ruling the generation mechanism. Specifically, we find a threshold excitation frequency governing the transition from the thermophone to the mechanophone mechanism. The role of the Kapitza resistance as a tuning parameter is unveiled. We then proved that the frequency-sweep analysis remains a good predictive tool also for the case of impulsive photoacoustic excitation triggered by a pulsed laser source.

The present results rationalize, on a formal basis, the physics behind recent numerical findings on impulsive acoustic excitation in nanofluids.[54,55,78,79] Furthermore, they allow revisiting, under a broader perspective, impulsive hypersonic acoustic wave generation in polymers,[103] and solid nanostructures,[104] triggered by heated solid nano-transducers. From an applicative stand-point, the mechanophone effect is of interest in bio-related applications requiring short acoustic wave generation while avoiding overheating the fluid. The mechanophone can potentially drive very short acoustic wavelengths in liquids, by activating the eigenmodes of the nanometric transducer. This will prove useful in developing local high-resolution acoustic imaging techniques. On the same footing, the mechanophone can be adopted to gain further insight into nanoparticle-fluid interactions at ultrahigh acoustic frequencies,[90] and to inspect the mechanical response of liquids in the hypersonic frequency range[105−110] and in glass-forming polymers.[111] In particular, this approach could be useful to elucidate the high-frequency collective dynamics in liquid water, marking a transition from ordinary or "slow" water, with sound velocity ≃1500 m/s, to "fast" water with a sound velocity ranging up to ≃3200 m/s. Indeed, in the THz frequency range, water might respond as a solid rather than a liquid, its dispersion becoming nonlinear and the sound velocity increasing to 3200 m/s.[112] This phenomenon has been predicted via molecular dynamic simulations and observed via inelastic x-ray scattering.[113−116] The mechanophone regime can be also useful to experimentally demonstrate dewetting during terahertz vibrations of nanoparticles. Indeed, molecular simulations proved the formation of a vacuum layer around a high-frequency vibrating nanoparticle in water.[117] Also, high-frequency thermoacoustic waves can induce a refractive index modulation with pressure and temperature in water,[118,119] which can be probed by detecting liquid resonances, e.g., by nanoplasmonics.[120] This effect could be exploited to realize realistic transduction systems, able to probe the water behavior in extreme conditions.[121]

In order to clarify the physical origin of the generation mechanisms, some simplifying assumptions were made, namely viscous phenomena and mechanical effects on heat propagation were disregarded. Neglecting viscous attenuation in the fluid limits the region of validity of the pressure waveform here reported. The pressure profile remains valid within a distance from the interface on the order of the acoustic penetration depth, which scales as ω^{-2}; see eq 13.[75,112] The model can be generalized to encompass the effect of fluid viscosity and of the mechanical response on the thermal one. Both aspects will make the object of prospective work.

https://doi.org/10.1021/acs.jpcc.3c01808
J. Phys. Chem. C 2023, 127, 10227−10244

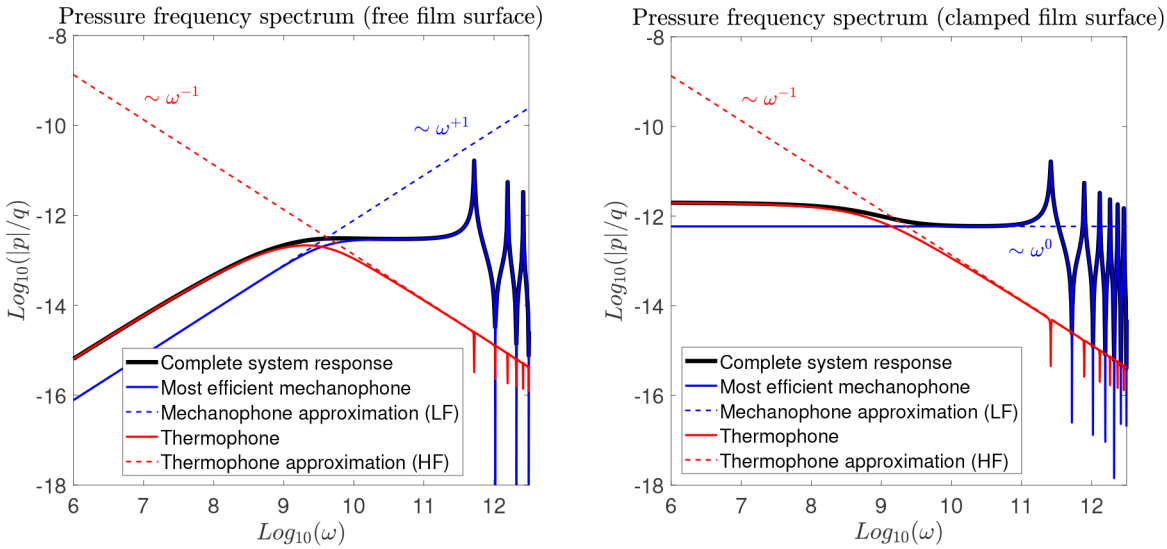

Figure 7. Comparison of the pressure spectrum of the system ($r = 3 \times 10^{-8}$ m^2·K/W) with the most efficient mechanophone ($r \to \infty$). Left panel: we compare the complete solution given by eq 45 (for $b = +1$ and $r = 3 \times 10^{-8}$ m^2 K/W, black curve) with the highest mechanophone efficiency ($r \to \infty$, blue curve) given in eq 93 and the thermophone solution given in eq 76 (for $b = +1$ and $r = 3 \times 10^{-8}$ m^2 K/W,red curve). We also show the low frequency (LF) approximation of the most efficient mechanophone response given in eq 94 (blue dashed curve) and the high frequency (HF) approximation of the thermophone response given in eq 79 (red dashed curve). Right panel: we compare the complete solution given by eq 45 (for $b = -1$ and $r = 3 \times 10^{-8}$ m^2 K/W, black curve)with the highest mechanophone efficiency ($r \to \infty$, blue curve) given in eq 97 and the thermophone solution given in eq 76 (for $b = -1$ and $r = 3 \times 10^{-8}$ m^2 K/W, red curve). We also show the low frequency (LF) approximation of the most efficient mechanophone response given in eq 98 (blue dashed curve) and the high frequency (HF) approximation of the thermophone response given in eq 79 (red dashed curve). Anti-resonances and quasi-resonances are given by the analysis developed in the Appendix.

APPENDIX: HIGHEST EFFICIENCY OF THE MECHANOPHONE MECHANISM

In this Appendix, we suppress the thermophone mechanism by considering a very large Kapitza resistance. So doing, we prevent the transit of heat from the solid to the fluid, and the only way left to generate the acoustic wave in the fluid is to exploit the oscillatory deformations of the solid. This represents the most efficient mechanophone since there is no heat lost in the fluid and all the energy input contributes to the expansion and compression of the solid, which through the piston effect, generates the wave in the fluid. We then apply the limiting condition $r \to \infty$, or equivalently, $S \to \infty$, as one can see from eq 53. Under this assumption, eqs 59, 60, and 61 simplify as follows

$$\xi = -\frac{B_1}{\rho_1}\frac{\alpha_1 q}{i\omega C_{p1}}, \tag{89}$$

$$\eta = 0, \tag{90}$$

$$\varphi = \frac{B_1}{\rho_1}\frac{\alpha_1 q}{i\omega C_{p1}}. \tag{91}$$

From these coefficients, we can determine the closed-form expression for the pressure within the fluid, i.e., for $x > L$

$$p(x) = e^{-\delta_0(x-L)}\frac{B_1\alpha_1 q}{i\omega\rho_1 C_{p1}} \times \frac{(e^{\delta_1 L} + be^{-\delta_1 L}) - (1+b)}{\sqrt{\frac{\rho_1 B_1}{\rho_0 B_0}}(e^{\delta_1 L} - be^{-\delta_1 L}) + (e^{\delta_1 L} + be^{-\delta_1 L})}, \tag{92}$$

where $b = \pm 1$ depends on the boundary condition used for $x = 0$. The spatial pressure decrease is not present because dissipative phenomena related to fluid viscosity have been neglected (δ_0 is purely imaginary). We separate the analysis for the two possible mechanical conditions at $x = 0$.

First, we consider the free surface condition at $x = 0$, characterized by $b = +1$. After straightforward algebra we get the pressure intensity $|p|$ for $x > L$ as

$$|p| = \frac{B_1\alpha_1 q}{\omega\rho_1 C_{p1}} \frac{1 - \cos\left(\omega\sqrt{\frac{\rho_1}{B_1}}L\right)}{\sqrt{\frac{\rho_1 B_1}{\rho_0 B_0}\sin^2\left(\omega\sqrt{\frac{\rho_1}{B_1}}L\right) + \cos^2\left(\omega\sqrt{\frac{\rho_1}{B_1}}L\right)}}, \tag{93}$$

where we considered the fact that δ_0 is a purely imaginary number and where, without limiting the generality, q is supposed to be real and positive. For low values of ω, we exploit the second order approximation $1 - \cos(x) \sim x^2/2$ ($x \ll 1$) for the numerator, whereas the square root in the denominator ~1. This leads to

$$|p| \simeq \frac{\alpha_1 q L^2}{2C_{p1}}\omega, \quad \omega \ll \frac{1}{L}\sqrt{\frac{B_1}{\rho 1.}} \tag{94}$$

The result stated in eq 93 is also useful to understand the physics occurring for high frequencies. Indeed, we can identify the anti-resonances that vanish the numerator (generating downward pressure peaks)

$$\omega_n^{a-r} = \frac{2n\pi}{L}\sqrt{\frac{B_1}{\rho_1}}, \quad n = 1, 2, 3, \ldots \tag{95}$$

and the quasi-resonances that minimize the denominator (it never vanishes identically but can take values close to zero that create upward pressure peaks)

https://doi.org/10.1021/acs.jpcc.3c01808
J. Phys. Chem. C 2023, 127, 10227−10244

$$\omega_n^{q-r} = \frac{(2n-1)\pi}{L}\sqrt{\frac{B_1}{\rho_1}}, \quad n = 1, 2, 3, \ldots \tag{96}$$

which can be easily identified in Figure 7 (left panel).

We can now perform the same analysis for the clamped surface condition at $x = 0$, corresponding to $b = -1$. In this case, the general result obtained in eq 92 delivers (for $x > L$)

$$|p| = \frac{\alpha_1 q\sqrt{\rho_0 B_0}L}{\rho_1 C_{p1}} \frac{\left|\frac{\sin\left(\omega\sqrt{\frac{\rho_1}{B_1}}L\right)}{\omega\sqrt{\frac{\rho_1}{B_1}}L}\right|}{\sqrt{\frac{\rho_0 B_0}{\rho_1 B_1}\sin^2\left(\omega\sqrt{\frac{\rho_1}{B_1}}L\right) + \cos^2\left(\omega\sqrt{\frac{\rho_1}{B_1}}L\right)}}. \tag{97}$$

In this case, we observe a plateau response for low frequencies described by

$$|p| \simeq \frac{\alpha_1 q\sqrt{\rho_0 B_0}L}{\rho_1 C_{p1}}, \quad \omega \ll \frac{1}{L}\sqrt{\frac{B_1}{\rho 1}}. \tag{98}$$

Concerning the high-frequency behavior, we can identify the anti-resonances

$$\omega_n^{a-r} = \frac{\pi n}{L}\sqrt{\frac{B_1}{\rho_1}}, \quad n = 1, 2, 3, \ldots \tag{99}$$

and the quasi-resonances

$$\omega_n^{q-r} = \left(n - \frac{1}{2}\right)\frac{\pi}{L}\sqrt{\frac{B_1}{\rho_1}}, \quad n = 1, 2, 3, \ldots \tag{100}$$

which can be easily identified in Figure 7 (right panel).

In Figure 7, we compare the pressure spectra of the system (for both free and clamped surfaces at $x = 0$) for $r = 3 \times 10^{-8}\cdot\mathrm{m}^2$ K/W against the highest mecanophone efficiency ($r = \infty$) and the purely thermophone response for $r = 3 \times 10^{-8}\cdot\mathrm{m}^2$ K/W. As already discussed for Figs. 2, we can identify the crossover between the two generation mechanisms. For $b = +1$ (free surface at $x = 0$), we compare the low frequency (LF) approximation of the highest mechanophone response given in eq 94 and the high frequency (HF) approximation of the thermophone response given in eq 79. The new frequency threshold turns out to be

$$\omega_\infty^*(b = +1) = \frac{1}{L}\sqrt{2\frac{\alpha_0}{\alpha_1}\frac{1}{r\rho_1}\frac{\sqrt{B_0\rho_0}}{\rho_0 C_{p0}}}, \tag{101}$$

and represents the frequency beyond which the mechanophone prevails when $b = +1$, as one can see in Figure 7 (left panel). We added the subscript ∞ to remind us that we are considering the highest efficiency of mechanophone with $r \to \infty$. For $b = -1$ (clamped surface at $x = 0$), we compare the low frequency (LF) approximation of the highest mechanophone response given in eq 98 and the high frequency (HF) approximation of the thermophone response given in eq 79. As before, we can determine the new frequency threshold, eventually obtaining

$$\omega_\infty^*(b = -1) = \frac{\alpha_0}{\alpha_1}\frac{1}{rL}\frac{1}{\rho_0 C_{p0}}, \tag{102}$$

and represents the frequency beyond which the mechanophone prevails when $b = -1$, as one can see in Figure 7 (right panel).

AUTHOR INFORMATION

Corresponding Authors

Stefano Giordano − *IEMN - Institut d'Électronique de Microélectronique et de Nanotechnologie, Université Lille, CNRS, Centrale Lille, Université Polytechnique Hauts-de-France, UMR 8520, F-59000 Lille, France;* orcid.org/0000-0003-4023-5384; Email: stefano.giordano@univ-lille.fr

Michele Diego − *Femto Nano Optics group, Université de Lyon, CNRS, Université Claude Bernard Lyon1, Institut Lumière Matière, F-69622 Villeurbanne, France; Institute of Industrial Science, The University of Tokyo, Tokyo 153-8505, Japan;* Email: michele.diego@univ-lyon1.fr

Francesco Banfi − *Femto Nano Optics group, Université de Lyon, CNRS, Université Claude Bernard Lyon1, Institut Lumière Matière, F-69622 Villeurbanne, France;* orcid.org/0000-0002-7465-8417; Email: francesco.banfi@univ-lyon1.fr

Complete contact information is available at: https://pubs.acs.org/10.1021/acs.jpcc.3c01808

Notes

The authors declare no competing financial interest.

ACKNOWLEDGMENTS

This work was partially supported by the LABEX iMUST (No. ANR-10-LABX-0064) of the Université de Lyon within the program "Investissements d'Avenir" (No. ANR-11-IDEX-0007). F.B. acknowledges financial support from the CNRS through Délégation CNRS 2022−2023.

REFERENCES

(1) Hunt, F. V. *Electroacoustics: The Analysis of Transduction, and its Historical Background*; Harvard University Press: Cambridge, MA, 1954.

(2) Curie, J.; Curie, P. Développement par pression de l'électricité polaire dans les cristaux hémièdres à faces inclinées. *Bulletin de Minéralogie* **1880**, *3-4*, 90−93.

(3) Lippman, G. Sur le principe de la conservation de l'électricité, ou second principe de la théorie des phénomènes électriques. *J. Phys. Theor. Appl.* **1881**, *10*, 381−394.

(4) Voigt, W. *Lehrbuch der Kristallphysik*; Teubner: Leipzig, 1910.

(5) Chilowsky, C. M.; Langévin, M. P. Procédés et appareils pour la production de signaux sous-marins dirigés et pour la localisation à distance d'obstacles sous-marins. French Patent No. 502913, 1916.

(6) Chilowsky, C. M.; Langévin, M. P. Production of submarine signals and the location of submarine objects. US Patent No. 1,471,547, 1917.

(7) Langévin, M. P. Procédé et appareils d'émission et de réception des ondes élastiques sous-marines à l'aide des propriétés piézo-électriques du quartz. French Patent No. 505703, 1918.

(8) Manbachi, A.; Cobbold, R. S. C. Development and application of piezoelectric materials for ultrasound generation and detection. *Ultrasound* **2011**, *19*, 187−196.

(9) Shung, K. K.; Cannata, J. M.; Zhou, Q. F. Piezoelectric materials for high frequency medical imaging applications: A review. *J. Electroceram.* **2007**, *19*, 141−147.

(10) Zhou, Q.; Lau, S.; Wu, D.; Kirk Shung, K. Piezoelectric films for high frequency ultrasonic transducers in biomedical applications. *Prog. Mater. Sci.* **2011**, *56*, 139−174.

(11) Fei, C.; Chiu, C. T.; Chen, X.; Chen, Z.; Ma, J.; Zhu, B.; Shung, K. K.; Zhou, Q. Ultrahigh Frequency (100 MHz-300 MHz) Ultrasonic Transducers for Optical Resolution Medical Imagining. *Sci. Rep.* **2016**, *6*, 28360.

(12) Salim, M. S.; Abd Malek, M. F.; Heng, R. B. W.; Juni, K. M.; Sabri, N. Capacitive micromachined ultrasonic transducers: Technology and application. *J. Med. Ultrasound* **2012**, *20*, 8−31.
(13) Nardi, D.; Travagliati, M.; Murnane, M.; Kapteyn, H.; Ferrini, G.; Giannetti, C.; Banfi, F. Impulsively Excited Surface Phononic Crystals: A Route Toward Novel Sensing Schemes. *IEEE Sens. J.* **2015**, *15*, 5142−5150.
(14) Nardi, D.; Zagato, E.; Ferrini, G.; Giannetti, C.; Banfi, F. Design of a surface acoustic wave mass sensor in the 100 GHz range. *Appl. Phys. Lett.* **2012**, *100*, 253106.
(15) Weisendanger, T. The thermophone. *Sci. Am. Suppl.* **1878**, *148*, 2353.
(16) de Lange, P. On thermophones. *Proc. R. Soc. London* **1915**, *91*, 239−241.
(17) Arnold, H. D.; Crandall, I. B. The thermophone as a precision source of sound. *Phys. Rev.* **1917**, *10*, 22−38.
(18) Wente, E. C. A condenser transmitter as a uniformly sensitive instrument for the absolute measurement of sound intensity. *Phys. Rev.* **1917**, *10*, 39−63.
(19) Wente, E. C. The thermophone. *Phys. Rev.* **1922**, *19*, 333−345.
(20) Bell, A. G. Upon the production of sound by radiant energy. *London, Edinburgh, and Dublin Philosophical Magazine and Journal of Science* **1881**, *11*, 510−528.
(21) Preece, W. H. I. On the conversion of radiant energy into sonorous vibrations. *Proc. R. Soc. London* **1881**, *31*, 506−520.
(22) Tyndall, J. III. Action of an intermittent beam of radiant heat upon gaseous matter. *Proc. R. Soc. London* **1881**, *31*, 307−317.
(23) Veingerov, M. L. Eine methode der gasanalyze beruhend auf dem optisch-akustischen Tyndall-Röntgeneffekt. *Dokl. Akad. Nauk SSSR* **1938**, *19*, 687−688.
(24) Gorelik, G. On a possible method of studying energy exchange times between the different degrees of freedom of molecules in a gas. *Dokl. Akad. Nauk SSSR* **1946**, *54*, 779.
(25) Harshbarger, W. R.; Robin, M. B. Opto-acoustic effect. Revival of an old technique for molecular spectroscopy. *Acc. Chem. Res.* **1973**, *6*, 329−334.
(26) Manohar, S.; Razansky, D. Photoacoustics: a historical review. *Adv. Opt. Photonics* **2016**, *8*, 586−617.
(27) Bertolotti, M.; Li Voti, R. A note on the history of photoacoustic, thermal lensing, and photothermal deflection techniques. *J. Appl. Phys.* **2020**, *128*, 230901.
(28) Shinoda, H.; Nakajima, T.; Ueno, K.; Koshida, N. Thermally induced ultrasonic emission from porous silicon. *Letters to Nature* **1999**, *400*, 853−855.
(29) Aliev, A. E.; Mayo, N. K.; Jung de Andrade, M.; Robles, R. O.; Fang, S.; Baughman, R. H.; Zhang, M.; Chen, Y.; Lee, J. A.; Kim, S. J. Alternative Nanostructures for Thermophones. *ACS Nano* **2015**, *9*, 4743−4756.
(30) Torraca, P.; Bobinger, M.; Servadio, M.; Pavan, P.; Becherer, M.; Lugli, P.; Larcher, L. On the Frequency Response of Nanostructured Thermoacoustic Loudspeakers. *Nanomaterials* **2018**, *8*, 833.
(31) Leizeronok, B.; Losin, S.; Kleiman, A.; Julius, S.; Romm, I.; Cukurel, B. Guidelines for higher efficiency supported thermo-acoustic emitters based on periodically Joule heated metallic films. *J. Acoust. Soc. Am.* **2023**, *153*, 1682−1693.
(32) Xiao, L.; Chen, Z.; Feng, C.; Liu, L.; Bai, Z. Q.; Wang, Y.; Qian, L.; Zhang, Y.; Li, Q.; Jiang, K.; et al. Flexible, stretchable, transparent carbon nanotube thin film loudspeakers. *Nano Lett.* **2008**, *8*, 4539−4545.
(33) Aliev, A. E.; Lima, M.; Fang, S.; Baughman, R. Underwater Sound Generation Using Carbon Nanotube Projectors. *Nano Lett.* **2010**, *10*, 2374−2380.
(34) Aliev, A. E.; Gartstein, Y. N.; Baughman, R. H. Increasing the efficiency of thermoacoustic carbon nanotube sound projectors. *Nanotechnology* **2013**, *24*, 235501.
(35) Aliev, A. E.; Mayo, N. K.; Baughman, R. H.; Avirovik, D.; Priya, S.; Zarnetske, M. R.; Blottman, J. B. Thermal management of thermoacoustic sound. *Nanotechnology* **2014**, *25*, 405704.
(36) Barnard, A. R.; Brungart, T. A.; McDevitt, T. E.; Aliev, A. E.; Jenkins, D. M.; Kline, B. L.; Baughman, R. H. Advancements toward a high-power, carbon nanotube, thin-film loudspeaker. *Noise Control Engineering Journal* **2014**, *62*, 360−367.
(37) Aliev, A. E.; Mayo, N. K.; Baughman, R. H.; Codoluto, D.; Ovalle-Robles, R.; Inoue, K.; Romanov, S. A.; Nasibulin, A. G.; et al. Thermoacoustic sound projector: exceeding the fundamental efficiency of carbon nanotubes. *Nanotechnology* **2018**, *29*, 325704.
(38) Wang, J.; Li, H.; Feng, Y.; Tong, Z.; Zhou, Z.; Xu, X.; Lim, C. W. New high fidelity (hi-fi) three-dimensional thermophone CNT sponge. *Extreme Mechanics Letters* **2021**, *49*, 101523.
(39) Niskanen, A.; Hassel, J.; Tikander, M.; Maijala, P.; Gronberg, L.; Helisto, P. Suspended metal wire array as a thermoacoustic sound source. *Appl. Phys. Lett.* **2009**, *95*, 163102.
(40) Dutta, R.; Albee, B.; Van Der Veer, W. E.; Harville, T.; Donovan, K. C.; Papamoschou, D.; Penner, R. M. Gold nanowire thermophones. *J. Phys. Chem. C* **2014**, *118*, 29101−29107.
(41) Tian, H.; Xie, D.; Yang, Y.; Ren, T. L.; Lin, Y. X.; Chen, Y.; Wang, Y. F.; Zhou, C. J.; Peng, P. G.; Wang, L. G.; et al. Flexible, ultrathin, and transparent sound-emitting devices using silver nanowires film. *Appl. Phys. Lett.* **2011**, *99*, 253507.
(42) Tian, H.; Ren, T. L.; Xie, D.; Wang, Y. F.; Zhou, C. J.; Feng, T. T.; Fu, D.; Yang, Y.; Peng, P. G.; Wang, L. G.; et al. Graphene-on-paper sound source devices. *ACS Nano* **2011**, *5*, 4878−4885.
(43) Fei, W.; Zhou, J.; Guo, W. Low-voltage Driven Graphene Foam Thermoacoustic Speaker. *Small* **2015**, *11*, 2252−2256.
(44) Kim, C. S.; Hong, S. K.; Lee, J. M.; Kang, D. S.; Cho, B. J.; Choi, J.W. Free-Standing Graphene Thermophone on a Polymer-Mesh Substrate. *Small* **2016**, *12*, 185−189.
(45) Tao, L.; Sun, H.; Liu, Y.; Ju, Z.; Yang, Y.; Ren, T. L. Flexible graphene sound device based on laser reduced graphene. *Appl. Phys. Lett.* **2017**, *111*, 103104.
(46) Ngoh, Z. L.; Guiraud, P.; Tan, D.; Giordano, S.; Bou-Matar, O.; Teo, E. H. T.; Pernod, P.; Coquet, P.; Lardat, R. Experimental characterization of three-dimensional Graphene's thermoacoustic response and its theoretical modelling. *Carbon* **2020**, *169*, 382−394.
(47) Ashton, T. S.; Moore, A. L. Three-dimensional foam-like hexagonal boron nitride nanomaterials via atmospheric pressure chemical vapor deposition. *J. Mater. Sci.* **2015**, *50*, 6220−6226.
(48) Loeblein, M.; Tay, R. Y.; Tsang, S. H.; Ng, W. B.; Teo, E. H. T. Configurable three-dimensional boron nitride-carbon architecture and its tunable electronic behavior with stable thermal performances. *Small* **2014**, *10*, 2992−2999.
(49) Emelianov, S. Y.; Li, P.; O'Donnell, M. Photoacoustics for molecular imaging and therapy. *Phys. Today* **2009**, *62*, 34−39.
(50) Xu, M.; Wang, L. V. Photoacoustic imaging in biomedicine. *Rev. Sci. Instrum.* **2006**, *77*, 041101.
(51) Li, C.; Wang, L. V. Photoacoustic tomography and sensing in biomedicine. *Phys. Med. Biol.* **2009**, *54*, R59−R97.
(52) Wang, L. V. *Photoacoustic imaging and spectroscopy*; CRC Press: Boca Raton, FL, 2017.
(53) Li, W.; Chen, X. Gold nanoparticles for photoacoustic imaging. *Nanomedicine* **2015**, *10*, 299−320.
(54) Prost, A.; Poisson, F.; Bossy, E. Photoacoustic generation by a gold nanosphere: From linear to nonlinear thermoelastics in the long-pulse illumination regime. *Phys. Rev. B* **2015**, *92*, 115450.
(55) Gandolfi, M.; Banfi, F.; Glorieux, C. Optical wavelength dependence of photoacoustic signal of gold nanofluids. *Photoacoustics* **2020**, *20*, 100199.
(56) Yang, X.; Stein, E. W.; Ashkenazi, S.; Wang, L. V. Nanoparticles for photoacoustic imaging. *Wiley Interdiscip. Rev.: Nanomed. Nanobiotechnol* **2009**, *1*, 360−368.
(57) Mantri, Y.; Jokerst, J. V. Engineering plasmonic nanoparticles for enhanced photoacoustic imaging. *ACS Nano* **2020**, *14*, 9408−9422.
(58) Luke, G. P.; Yeager, D.; Emelianov, S. Y. Biomedical applications of photoacoustic imaging with exogenous contrast agents. *Ann. Biomed. Eng.* **2012**, *40*, 422−437.
(59) Williams, D. F. On the mechanisms of biocompatibility. *Biomaterials* **2008**, *29*, 2941−2953.

https://doi.org/10.1021/acs.jpcc.3c01808
J. Phys. Chem. C 2023, 127, 10227−10244

(60) Carnovale, C.; Bryant, G.; Shukla, R.; Bansal, V. Identifying Trends in Gold Nanoparticle Toxicity and Uptake: Size, Shape, Capping Ligand, and Biological Corona. *ACS Omega* **2019**, *4*, 242−256.
(61) Parker, J. G. Optical Absorption in Glass: Investigation Using an Acoustic Technique. *Appl. Opt.* **1973**, *12*, 2974−2977.
(62) Rosencwaig, A.; Gersho, A. Photoacoustic Effect with Solids: A Theoretical Treatment. *Science* **1975**, *190*, 556−557.
(63) Rosencwaig, A.; Gersho, A. Theory of the photoacoustic effect with solids. *J. Appl. Phys.* **1976**, *47*, 64−69.
(64) McDonald, F. A.; Wetsel, G. C. Generalized theory of the photoacoustic effect. *J. Appl. Phys.* **1978**, *49*, 2313.
(65) Daschewski, M.; Boehm, R.; Prager, J.; Kreutzbruck, M.; Harrer, A. Physics of thermo-acoustic sound generation. *J. Appl. Phys.* **2013**, *114*, 114903.
(66) Daschewski, M.; Kreutzbruck, M.; Prager, J. Influence of thermodynamic properties of a thermo-acoustic emitter on the efficiency of thermal airborne ultrasound generation. *Ultrasonics* **2015**, *63*, 16−22.
(67) La Torraca, P.; Larcher, L.; Bobinger, M.; Pavan, P.; Seeber, B.; Lugli, P. Physical modeling and characterization of thermo-acoustic loudspeakers made of silver nano-wire films. *J. Appl. Phys.* **2017**, *121*, 214502.
(68) Hu, H.; Zhu, T.; Xu, J. Model for thermoacoustic emission from solids. *Appl. Phys. Lett.* **2010**, *96*, 214101.
(69) Vesterinen, V.; Niskanen, A. O.; Hassel, J.; Helisto, P. Fundamental efficiency of nanothermophones: Modeling and experiments. *Nano Lett.* **2010**, *10*, 5020−5024.
(70) Hu, H.; Wang, Z.; Wu, H.; Wang, Y. Analysis of spherical thermo-acoustic radiation in gas. *AIP Advances* **2012**, *2*, 032106.
(71) Hu, H.; Wang, Y.; Wang, Z. Wideband flat frequency response of thermo-acoustic emission. *J. Phys. D: Appl. Phys.* **2012**, *45*, 345401.
(72) Lim, C. W.; Tong, L. H.; Li, Y. C. Theory of suspended carbon nanotube thin film as a thermal-acoustic source. *Journal of Sound and Vibration* **2013**, *332*, 5451−5461.
(73) Hu, H.; Wang, D.; Wang, Z. Solution for acoustic field of thermo-acoustic emission from arbitrary source. *AIP Advances* **2014**, *4*, 107114.
(74) Yin, Y.; Hu, H. Analysis of cylindrical thermo-acoustic radiation in gas. *AIP Conf. Proc.* **2017**, *1829*, 020033.
(75) Guiraud, P.; Giordano, S.; Bou-Matar, O.; Pernod, P.; Lardat, R. Multilayer modeling of thermoacoustic sound generation for thermophone analysis and design. *Journal of Sound and Vibration* **2019**, *455*, 275−298.
(76) Guiraud, P.; Giordano, S.; Bou-Matar, O.; Pernod, P.; Lardat, R. Two temperature model for thermoacoustic sound generation in thick porous thermophones. *J. Appl. Phys.* **2019**, *126*, 165111.
(77) Guiraud, P.; Giordano, S.; Bou-Matar, O.; Pernod, P.; Lardat, R. Thermoacoustic wave generation in multilayered thermophones with cylindrical and spherical geometries. *J. Appl. Phys.* **2021**, *129*, 115103.
(78) Diego, M.; Gandolfi, M.; Casto, A.; Bellussi, F. M.; Vialla, F.; Crut, A.; Roddaro, S.; Fasano, M.; Vallée, F.; Del Fatti, N.; et al. Ultrafast nano generation of acoustic waves in water via a single carbon nanotube. *Photoacoustics* **2022**, *28*, 100407.
(79) Diego, M.; Gandolfi, M.; Giordano, S.; Vialla, F.; Crut, A.; Vallée, F.; Maioli, P.; Del Fatti, N.; Banfi, F. Tuning photoacoustics with nanotransducers via thermal boundary resistance and laser pulse duration. *Appl. Phys. Lett.* **2022**, *121*, 252201.
(80) Chen, J.; Xu, X.; Zhou, J.; Li, B. Interfacial thermal resistance: Past, present, and future. *Rev. Mod. Phys.* **2022**, *94*, 025002.
(81) Landau, L. D.; Lifschitz, E. M. *Fluid Mechanics, Course of Theoretical Physics*; Butterworths Heinemann: Oxford, U.K., 1986; Vol. 6.
(82) Landau, L. D.; Lifschitz, E. M. *Theory of Elasticity, Course of Theoretical Physics*; Butterworths Heinemann: Oxford, U.K., 1986; Vol. 7.
(83) Schulz, J. C. F.; Schlaich, A.; Heyden, M.; Netz, R. R.; Kappler, J. Molecular interpretation of the non-Newtonian viscoelastic behavior of liquid water at high frequencies. *Phys. Rev. Fluids* **2020**, *5*, 103301.
(84) Kapitza, P. L. *Collected Papers of P. L. Kapitza*; Pergamon: Oxford, U.K., 1964; Vol. 3.
(85) Torquato, S.; Rintoul, M. D. Effect of the Interface on the Properties of Composite Media. *Phys. Rev. Lett.* **1995**, *75*, 4067. Levine, G.; Howard, J. Erratum: Macroscopic Quantum Coherence and Quasidegeneracy in Antiferromagnets. *Phys. Rev. Lett.* **1996**, *76*, 3241.
(86) Pavanello, F.; Manca, F.; Luca Palla, P.; Giordano, S. Generalized interface models for transport phenomena: Unusual scale effects in composite nanomaterials. *J. Appl. Phys.* **2012**, *112*, 084306.
(87) Pavanello, F.; Giordano, S. How imperfect interfaces affect the nonlinear transport properties in composite nanomaterials. *J. Appl. Phys.* **2013**, *113*, 154310.
(88) Yu, H.-Q.; Yao, J.; Wu, X.-W.; Wu, D.-J.; Liu, X.-J. Tunable photoacoustic properties of gold nanoshells with near-infrared optical responses. *J. Appl. Phys.* **2017**, *122*, 134901.
(89) Sun, J.-P.; Ren, Y.-T.; Wei, K.; He, M.-J.; Gao, B.-H.; Qi, H. Photoacoustic response optimization of gold nanorods in the near-infrared region. *Results Phys.* **2022**, *34*, 105209.
(90) Yu, K.; Yang, Y.; Wang, J.; Hartland, G. V.; Wang, G. P. Nanoparticle-Fluid Interactions at Ultrahigh Acoustic Vibration Frequencies Studied by Femtosecond Time-Resolved Microscopy. *ACS Nano* **2021**, *15*, 1833−1840.
(91) Wang, C.; Kan, C.; Zhu, J.; Zeng, X.; Wang, X.; Li, H.; Shi, D. Synthesis of high-yield gold nanoplates: fast growth assistant with binary surfactants. *J. Nanomater.* **2010**, *2010*, 1.
(92) Krauss, E.; Kullock, R.; Wu, X.; Geisler, P.; Lundt, N.; Kamp, M.; Hecht, B. Controlled growth of high-aspect-ratio single-crystalline gold platelets. *Cryst. Growth Des.* **2018**, *18*, 1297−1302.
(93) Wilson, B. A.; Nielsen, S. O.; Randrianalisoa, J. H.; Qin, Z. Curvature and temperature-dependent thermal interface conductance between nanoscale gold and water. *J. Chem. Phys.* **2022**, *157*, 054703.
(94) Herrero, C.; Joly, L.; Merabia, S. Ultra-high liquid−solid thermal resistance using nanostructured gold surfaces coated with graphene. *Appl. Phys. Lett.* **2022**, *120*, 171601.
(95) Noll, F.; Krauß, N.; Gusev, V.; Dekorsy, T.; Hettich, M. Surface Plasmon-Based Detection for Picosecond Ultrasonics in Planar Gold-Dielectric Layer Geometries. *Photoacoustics* **2023**, *30*, 100464.
(96) Rizzi, G.; Benetti, G.; Giannetti, C.; Gavioli, L.; Banfi, F. Analytical model of the acoustic response of nanogranular films adhering to a substrate. *Phys. Rev. B* **2021**, *104*, 035416.
(97) Muskens, O. L.; Del Fatti, N.; Vallée, F. Femtosecond response of a single metal nanoparticle. *Nano Lett.* **2006**, *6*, 552−556.
(98) Rosenblatt, G.; Simkhovich, B.; Bartal, G.; Orenstein, M. Nonmodal Plasmonics: Controlling the Forced Optical Response of Nanostructures. *Phys. Rev. X* **2020**, *10*, 011071.
(99) Hale, G. M.; Querry, M. R. Optical constants of water in the 200-nm to 200-μ m wavelength region. *Applied Optics* **1973**, *12*, 555−563.
(100) Abeles, F. Optical Properties of very thin films. *Thin Solid Films* **1976**, *34*, 291−302.
(101) Wright, O. B.; Gusev, V. E. Ultrafast acoustic phonon generation in gold. *Phys. B (Amsterdam, Neth.)* **1996**, *220*, 770−772.
(102) Hohlfeld, J.; Wellershoff, S.; Gudde, J.; Conrad, U.; Jahnke, V.; Matthias, E. Electron and lattice dynamics following optical excitation of metals. *Chem. Phys.* **2000**, *251*, 237−258.
(103) Travagliati, M.; Nardi, D.; Giannetti, C.; Gusev, V.; Pingue, P.; Piazza, V.; Ferrini, G.; Banfi, F. Interface Nano-Confined Acoustic Waves in Polymeric Surface Phononic Crystals. *Appl. Phys. Lett.* **2015**, *106*, 021906.
(104) Gandolfi, M.; Peli, S.; Diego, M.; Danesi, S.; Giannetti, C.; Alessandri, I.; Zannier, V.; Demontis, V.; Rocci, M.; Beltram, F.; et al. Ultrafast Photoacoustic Nanometrology of InAs Nanowires Mechanical Properties. *J. Phys. Chem. C* **2022**, *126*, 6361−6372.
(105) Pelton, M.; Chakraborty, D.; Malachosky, E.; Guyot-Sionnest, P.; Sader, J. E. Viscoelastic Flows in Simple Liquids Generated by Vibrating Nanostructures. *Phys. Rev. Lett.* **2013**, *111*, 244502.
(106) Yu, K.; Major, T. A.; Chakraborty, D.; Devadas, M. S.; Sader, J. E.; Hartland, G. V. Compressible Viscoelastic Liquid Effects Generated by the Breathing Modes of Isolated Metal Nanowires. *Nano Lett.* **2015**, *15*, 3964−3970.

https://doi.org/10.1021/acs.jpcc.3c01808
J. Phys. Chem. C 2023, 127, 10227−10244

(107) Galstyan, V.; Pak, O. S.; Stone, H. A. A Note on the Breathing Mode of an Elastic Sphere in Newtonian and Complex Fluids. *Phys. Fluids* **2015**, *27*, 032001.
(108) Chakraborty, D.; Sader, J. E. Constitutive Models for Linear Compressible Viscoelastic Flows of Simple Liquids at Nanometer Length Scales. *Phys. Fluids* **2015**, *27*, 052002.
(109) Marty, R.; Arbouet, A.; Girard, C.; Mlayah, A.; Paillard, V.; Lin, V. K.; Teo, S. L.; Tripathy, S. Damping of the Acoustic Vibrations of Individual Gold Nanoparticles. *Nano Lett.* **2011**, *11*, 3301−3306.
(110) Benetti, G.; Gandolfi, M.; Van Bael, M. J.; Gavioli, L.; Giannetti, C.; Caddeo, C.; Banfi, F. Photoacoustic sensing of trapped fluids in nanoporous thin films: device engineering and sensing scheme. *ACS Appl. Mater. Interfaces* **2018**, *10*, 27947−27954.
(111) Brick, D.; Hofstetter, M.; Stritt, P.; Rinder, J.; Gusev, V.; Dekorsy, T.; Hettich, M. Glass transition of nanometric polymer films probed by picosecond ultrasonics. *Ultrasonics* **2022**, *119*, 106630.
(112) Ruocco, G.; Sette, F. The history of the fast sound in liquid water. *Condens. Matter Phys.* **2008**, *11*, 29−46.
(113) Sciortino, F.; Sastry, S. Sound propagation in liquid water: The puzzle continues. *J. Chem. Phys.* **1994**, *100*, 3881−3893.
(114) Sette, F.; Ruocco, G.; Krisch, M.; Masciovecchio, C.; Verbeni, R.; Bergmann, U. Transition from Normal to Fast Sound in Liquid Water. *Phys. Rev. Lett.* **1996**, *77*, 83−86.
(115) Ruocco, G.; Sette, F. The high-frequency dynamics of liquid water. *J. Phys.: Condens. Matter* **1999**, *11*, R259−R293.
(116) Mallamace, F.; Corsaro, C.; Stanley, H. E. Possible relation of water structural relaxation to water anomalies. *Proc. Natl. Acad. Sci. U. S. A.* **2013**, *110*, 4899−4904.
(117) Hsueh, C.-C.; Gordon, R.; Rottler, J. Dewetting during Terahertz Vibrations of Nanoparticles. *Nano Lett.* **2018**, *18*, 773−777.
(118) Ellison, W. J. Permittivity of Pure Water, at Standard Atmospheric Pressure, over the Frequency Range 0-25 THz and the Temperature Range 0-100 °C. *J. Phys. Chem. Ref. Data* **2007**, *36*, 1−18.
(119) Titov, S. V.; Coffey, W. T.; Dowling, W. J.; Zarifakis, M.; Kalmykov, Y. P.; Titov, A. S. Anomalous diffusion of molecules with rotating polar groups: The joint role played by inertia and dipole coupling in microwave and far-infrared absorption. *Phys. Rev. E* **2020**, *102*, 052130.
(120) Wang, Y.; Wu, J.; Moradi, S.; Gordon, R. Generating and Detecting High-Frequency Liquid-Based Sound Resonances with Nanoplasmonics. *Nano Lett.* **2019**, *19*, 7050−7053.
(121) Pan, D.; Spanu, L.; Harrison, B.; Sverjensky, D. A.; Galli, G. Dielectric properties of water under extreme conditions and transport of carbonates in the deep Earth. *Proc. Natl. Acad. Sci. U. S. A.* **2013**, *110*, 6646−6650.

https://doi.org/10.1021/acs.jpcc.3c01808
J. Phys. Chem. C 2023, 127, 10227−10244